



AMERICAN METEOROLOGICAL SOCIETY

Journal of Climate

EARLY ONLINE RELEASE

This is a preliminary PDF of the author-produced manuscript that has been peer-reviewed and accepted for publication. Since it is being posted so soon after acceptance, it has not yet been copyedited, formatted, or processed by AMS Publications. This preliminary version of the manuscript may be downloaded, distributed, and cited, but please be aware that there will be visual differences and possibly some content differences between this version and the final published version.

The DOI for this manuscript is doi: 10.1175/JCLI-D-16-0890.1

The final published version of this manuscript will replace the preliminary version at the above DOI once it is available.

If you would like to cite this EOR in a separate work, please use the following full citation:

Michel, C., A. Terpstra, and T. Spengler, 2017: Polar Mesoscale Cyclone Climatology for the Nordic Seas based on the ERA-Interim Reanalysis. *J. Climate*. doi:10.1175/JCLI-D-16-0890.1, in press.

© 2017 American Meteorological Society



Polar Mesoscale Cyclone Climatology for the Nordic Seas based on the ERA-Interim Reanalysis

Clio Michel*

Geophysical Institute, University of Bergen and Bjerknes Centre for Climate Research, Bergen,
Norway

Annick Terpstra

Geophysical Institute, University of Bergen and Bjerknes Centre for Climate Research, Bergen,
Norway

Thomas Spengler

Geophysical Institute, University of Bergen and Bjerknes Centre for Climate Research, Bergen,
Norway

¹²*Corresponding author address: Geophysical Institute, University of Bergen, Postboks 7803, 5020
Bergen, Norway.

¹⁴E-mail: Clio.Michel@uib.no

ABSTRACT

15 Polar mesoscale cyclones (PMCs) are automatically detected and tracked
16 over the Nordic seas using the Melbourne University algorithm applied to
17 the ERA-Interim reanalysis. The novelty of this study lies in the length of
18 the dataset (1979-2014), the usage of PMC tracks to infer relationships to
19 large-scale flow patterns, and elucidating the sensitivity to different selection
20 criteria when defining PMCs and polar lows and their genesis environments.

21 The angle between the ambient mean and thermal wind is used to distin-
22 guish two different PMCs genesis environments. The forward shear environ-
23 ment (thermal and mean wind in same direction) features typical baroclinic
24 conditions with a temperature gradient at the surface and a strong jet stream
25 at the tropopause. The reverse shear environment (thermal and mean wind in
26 opposite direction) features an occluded cyclone with a barotropic structure
27 throughout the entire troposphere and a low-level jet.

28 In contrast to previous studies, PMC occurrence does neither feature a sig-
29 nificant trend nor a significant link with the North Atlantic Oscillation and the
30 Scandinavian Blocking (SB), though the SB negative pattern seems to pro-
31 mote reverse shear PMC genesis. The sea ice extent in the Nordic seas is not
32 associated with overall changes in PMC occurrence but influences the genesis
33 location. Selected cold air outbreak indices and the temperature difference be-
34 tween the sea surface and 500 hPa (SST-T500) show no robust link with PMC
35 occurrence but the characteristics of forward shear PMCs and their synoptic
36 environments are sensitive to the choice of the SST-T500 threshold.

37 **1. Introduction**

38 Polar mesoscale cyclones (PMCs) are cyclonic systems with a horizontal extent less than 1000
39 km and a lifetime of about one day (Rasmussen and Turner 2003). They occur poleward of the
40 polar front, over maritime areas, in both hemispheres, and mainly during the cold season. The
41 most intense PMCs, referred to as polar lows, are associated with cold air outbreaks (CAOs) and
42 feature strong winds (e.g., Businger 1985; Harold et al. 1999a; Rasmussen and Turner 2003). The
43 least intense systems do neither feature an organized cloud signature nor a well defined pressure
44 minimum. Most of previous climatological studies have focused on polar lows (e.g., Wilhelmsen
45 1985; Ese et al. 1988; Harold et al. 1999a; Blechschmidt 2008; Bracegirdle and Gray 2008; Zahn
46 and von Storch 2008; Noer et al. 2011; Zappa et al. 2014) and a few on PMCs (e.g., Carrasco
47 and Bromwich 1992; Turner and Thomas 1994; Harold et al. 1999a,b; Condron et al. 2006; Irving
48 et al. 2010). Climatologies over the Nordic seas (Greenland, Norwegian, and Barents seas) con-
49 sidered rather short periods up to 12 years (Wilhelmsen 1985; Ese et al. 1988; Harold et al. 1999a;
50 Condron et al. 2006; Blechschmidt 2008; Bracegirdle and Gray 2008; Noer et al. 2011; Zappa
51 et al. 2014), with the exception of Zahn and von Storch (2008), who provided polar low track
52 density maps covering four decades using dynamically downscaled data. Businger (1985, 1987)
53 and Chen and von Storch (2013) showed that the characteristics and identification criteria of polar
54 lows differ between the North Atlantic and Pacific. Moreover, PMCs over the Nordic seas have
55 a strong influence on oceanic deep convection and hence on the Atlantic meridional overturning
56 circulation (Condron and Renfrew 2013). Therefore, we focus on the Nordic seas and use PMC
57 tracks obtained from reanalysis data over several decades to compile a climatology and investigate
58 the genesis environments, evolution characteristics, and linkages to large-scale circulation patterns
59 as well as sea ice extent.

60 Climatological studies of polar lows in the Norwegian and Barents seas have been performed by
61 manually tracking polar lows on weather maps (Wilhelmsen 1985; Businger 1985; Ese et al. 1988)
62 and satellite images (Forbes and Lottes 1985; Yarnal and Henderson 1989; Harold et al. 1999a;
63 Mokhov et al. 2007; Blechschmidt 2008), or by using a combination of these two methods (Noer
64 et al. 2011). Polar lows and PMCs have also been detected and tracked using automatic algorithms
65 applied to reanalysis and downscaled reanalysis (Condron et al. 2006; Zahn and von Storch 2008;
66 Chen and von Storch 2013; Zappa et al. 2014; Yanase et al. 2016). These algorithms apply sev-
67 eral criteria to distinguish between polar lows and other cyclonic features. One commonly used
68 criterion is low-level static stability defined as the difference between the sea surface temperature
69 (SST) and the 500-hPa temperature. Typical threshold values are 39 or 43 K, depending on the
70 area of interest, to identify environments conducive for convection and hence polar low genesis.
71 Another criterion is a southward propagation direction for polar lows (Zahn and von Storch 2008;
72 Chen and von Storch 2013). However, recent studies have shown that these criteria and thresholds
73 are problematic and potentially bias polar low climatologies toward specific polar low types and
74 environments (Rojo et al. 2015; Terpstra et al. 2016; Yanase et al. 2016). As all types of mesoscale
75 cyclones are relevant to assess their potential impact on the climate system, we aim to avoid these
76 shortcomings by considering the full spectrum of mesoscale cyclones for our climatology (section
77 2).

78 As indicated above, most of the previous climatologies do not cover more than one decade, lim-
79 iting the statistical robustness of track density maps as well as genesis and lysis locations. These
80 shorter-term climatologies are also inadequate to investigate inter-annual variability and long-term
81 trends in PMC occurrence. For example, Zahn and von Storch (2008) did not find any trends in
82 polar low occurrence for the period 1948-2006, whereas Rojo et al. (2015) indicated an increasing
83 number of polar lows during the years 2005-2013. Given the limited statistical robustness and

84 inability to investigate inter-annual or long-term trends, there is a need for more consistent cli-
85 matologies for both PMCs and polar lows to resolve these issues. We use the European Centre
86 for Medium-Range Weather Forecast (ECMWF) Interim reanalysis (ERA-I) from 1979 to 2014.
87 However, due to the sometimes inadequate representation of polar lows in ERA-I (Zappa et al.
88 2014), we will focus on all types of PMCs and present their track densities together with their
89 genesis and lysis densities (section 3).

90 Duncan (1978) hypothesized that polar lows can form in an environment that he coined “reverse
91 shear”, which refers to atmospheric conditions where the mean and thermal wind in the tropo-
92 sphere have opposite directions. In contrast, the environment is referred to as “forward shear”
93 when the mean wind has the same direction as the thermal wind. Using the 10-year Sea surface
94 Temperature and AltimeteR Synergy for improved forecasting of polar lows database (STARS¹,
95 Sætra et al. 2010), Terpstra et al. (2016) showed that reverse and forward shear polar low gene-
96 sis environments can be objectively distinguished using the wind shear condition. In agreement
97 with Blechschmidt (2008), they found that about 20% of polar lows in the Nordic seas form in
98 reverse shear conditions. Furthermore, they pinpointed that the synoptic conditions for forward
99 and reverse shear are in stark contrast, with synoptic conditions for reverse shear comprising an
100 occluded cyclone with a low-level jet at the genesis location, whereas the synoptic conditions for
101 forward shear resemble the typical baroclinic environment in which mid-latitude cyclones develop
102 (Terpstra et al. 2016). We extend the previous 10-year study and present environments for PMCs
103 forming in forward and reverse shear conditions for the ERA-I period 1979-2014. In addition,
104 we investigate the spatial and temporal distribution as well as the evolution of PMCs in these two
105 distinct conditions (section 4).

¹Provides polar low tracks from 2002 to 2011 over the Norwegian Sea (<http://polarlow.met.no/stars/>).

106 As PMCs are often not adequately resolved in coarser reanalyses and climate simulations, sev-
107 eral studies used large-scale circulation patterns associated with potentially favourable environ-
108 ments for polar low formation as a proxy for polar low occurrence (e.g., Kolstad 2006; Claud et al.
109 2007; Kolstad et al. 2009). Claud et al. (2007) argued that both the negative and positive phase of
110 the North Atlantic Oscillation (NAO- and NAO+) are environments conducive for polar low devel-
111 opment. Using actual tracks, however, Mallet et al. (2013) demonstrated that the NAO+ was more
112 conducive to polar low development than NAO-. Claud et al. (2007) and Mallet et al. (2013) agree
113 that polar lows tend to form during the counter pattern of Scandinavian Blocking (SB). Kolstad
114 (2006) and Kolstad et al. (2009) associated polar low occurrence to the presence of CAOs, due to
115 the reduced low-level stability and potential for convective development during CAOs. However,
116 thus far only Mallet et al. (2013) verified the correspondence of large-scale patterns with actual
117 polar low tracks based on shorter-term climatologies and the association of polar lows with CAO
118 indices has not been evaluated, yet. We will use our long-term PMC track dataset to investigate
119 the large-scale genesis environment as well as linkages between PMC occurrence and the NAO,
120 SB, CAO indices, and sea-ice extent (section 5).

121 2. Data and methods

122 a. Data

123 We use the ERA-I reanalysis generated with the ECMWF Integrated Forecast System model us-
124 ing a 4D-Var data assimilation scheme (Dee et al. 2011). We used data interpolated to $0.5^\circ \times 0.5^\circ$
125 horizontal resolution and with a 6-hour temporal resolution for the months October to April for
126 the period 1979-2014, resulting in 35 extended winters. Condron et al. (2006) automatically de-
127 tected PMCs in the ECMWF 40-year reanalysis (ERA-40, Uppala et al. 2005) and compared them

128 to PMCs detected on satellite images. They found that the largest PMCs are well represented in
129 ERA-40 but that the data assimilation biased the location of some PMCs. Laffineur et al. (2014)
130 compared the representation of polar lows in the ERA-I reanalysis with the ERA-40 reanalysis,
131 showing that ERA-I features more polar lows than ERA-40. Furthermore, Zappa et al. (2014)
132 were able to objectively track 55% of the STARS polar lows in ERA-I and showed that there are
133 even more polar lows in ERA-I with counterparts in STARS. They did not detect these additional
134 polar lows due to their chosen thresholds in vorticity and wind speed, the latter known to be un-
135 derestimated in ERA-I (e.g., Moore et al. 2015). Hence, ERA-I seems a suitable reanalysis dataset
136 to objectively detect a significant fraction of PMCs and to characterise their genesis environment
137 and evolution characteristics.

138 *b. Polar mesoscale cyclone tracks*

139 1) CYCLONE DETECTION AND TRACKING ALGORITHM

140 We employ the Melbourne University detection and tracking algorithm (Murray and Simmonds
141 1991a,b), which uses the maximum of the Laplacian of the mean sea level pressure (MSLP) to
142 detect cyclones. We only retain smaller scale systems (less than \sim 800 km diameter) by apply-
143 ing a weak smoothing of the MSLP Laplacian together with low thresholds in MSLP Laplacian
144 maximum averaged over a small radius of 1.25 degrees latitude². Once the cyclones are located
145 they are tracked in time. The tracking combines cyclones of two consecutive timesteps using the
146 nearest-neighbor method and the most likely propagation direction determined with the previous
147 movement and the steering velocity. A probability is calculated for all possible combinations of
148 tracks and only the track with the largest total probability is kept (see Murray and Simmonds
149 1991a,b, for more details). The values used in the algorithm's namelists are shown in Table A1.

²The detection and tracking algorithm uses the unit of degree latitude, which is about 111 km.

150 2) SELECTION OF POLAR MESOSCALE CYCLONE TRACKS

151 Several studies pointed out that the criteria to select polar lows, such as the stability criterion
152 using the difference between SST and temperature at 500 hPa, low-level wind, as well as restricting
153 polar low propagation to be only southward, appear problematic (Zappa et al. 2014; Terpstra et al.
154 2016; Smirnova and Golubkin 2017). To avoid any a priori bias in our dataset, we keep the full
155 range of PMCs by applying the selection criteria listed below:

- 156 • Minimum duration of 12 hours,
- 157 • Minimum of MSLP along each track within 1 October to 30 April from 1979 to 2014,
- 158 • Genesis and lysis location within (20°W-60°E/60°N-85°N),
- 159 • At least 50% of the grid points in a 200-km radius around the genesis location over sea or sea
160 ice,
- 161 • Laplacian of MSLP averaged over a radius of 1.25 degree latitude greater than 1 hPa per
162 degree latitude squared for at least one time step along the track,
- 163 • Distance between genesis and lysis greater than 300 km,
- 164 • Tracks are discontinued when reaching land or when the distance between two consecutive
165 points is greater than 350 km.

166 We end up with 8518 tracks for the 35 extended winters, that is 243 PMCs per extended winter
167 on average. Even though this number might appear high, we argue it is reasonable given the
168 selection criteria applied here. A comparison of our selected tracks with the tracks of the STARS
169 database yields a match of about 60%, compared to 55% in Zappa et al. (2014), who used the
170 3-hour forecast between the 6 hourly-analysis times of ERA-I reanalyses.

171 *c. Forward and reverse shear conditions*

172 We use the method based on Kolstad (2006) and Terpstra et al. (2016) to determine the angle
 173 between the mean wind and the thermal wind, where the mean wind $\mathbf{V}_m = (u_m, v_m)$ is the vertically
 174 averaged geostrophic wind between 925 and 700 hPa,

$$\mathbf{V}_m = \left(-\frac{1}{2f} \left(\frac{\partial \phi_{700}}{\partial \varphi} + \frac{\partial \phi_{925}}{\partial \varphi} \right), \frac{1}{2f} \left(\frac{\partial \phi_{700}}{a \cos \varphi \partial \lambda} + \frac{\partial \phi_{925}}{a \cos \varphi \partial \lambda} \right) \right), \quad (1)$$

175 where ϕ_{700} and ϕ_{925} are the geopotential at 700 and 925 hPa, respectively, f is the Coriolis parameter,
 176 a the Earth's radius, λ the longitude, and φ the latitude. The thermal wind $\mathbf{V}_T = (u_T, v_T)$ is
 177 defined between the same pressure levels

$$\mathbf{V}_T = \left(-\frac{1}{f} \frac{\partial (\phi_{700} - \phi_{925})}{a \partial \varphi}, \frac{1}{f} \frac{\partial (\phi_{700} - \phi_{925})}{a \cos \varphi \partial \lambda} \right). \quad (2)$$

178 Finally, the angle α between the two vectors is calculated

$$\alpha = \arccos \left(\frac{\mathbf{V}_T \cdot \mathbf{V}_m}{\|\mathbf{V}_T\| \|\mathbf{V}_m\|} \right), \quad (3)$$

179 which is averaged over a radius of 200 km around the genesis point.

180 Following Terpstra et al. (2016), we consider the environment at the genesis time around the
 181 genesis point as forward (reverse) shear if $0^\circ \leq \alpha \leq 45^\circ$ ($135^\circ \leq \alpha \leq 180^\circ$). Based on these
 182 thresholds, 2002 out of 8518 PMCs (24%) form in forward shear conditions and 800 PMCs (9%)
 183 form in reverse shear conditions. These percentages are different from Terpstra et al. (2016) who
 184 found about 20% of polar lows in both categories in the STARS database. Hence, our dataset
 185 contains a larger fraction of PMCs developing in forward shear conditions compared to the polar
 186 lows in the STARS database.

187 Following Terpstra et al. (2016), we also investigate the relation between α and the vertical wind
 188 speed gradient between 925 and 700 hPa, where the latter is defined as

$$\frac{dV}{dz} = g \frac{V_{700} - V_{925}}{\phi_{700} - \phi_{925}}, \quad (4)$$

189 with geopotential ϕ , $V_{700} = \sqrt{u_{700}^2 + v_{700}^2}$ and $V_{925} = \sqrt{u_{925}^2 + v_{925}^2}$ with u and v the zonal and
190 meridional components of the wind, respectively, and gravity $g = 9.80665 \text{ m s}^{-2}$. When the wind
191 speed increases with altitude, the thermal wind relation states that the cold (warm) air resides to
192 the left (right) side of the mean wind, which induces a thermal wind in the same direction as the
193 mean wind, hence the low angle (Fig. 2). On the other hand, when the wind speed decreases with
194 altitude, the thermal wind relation states that the cold (warm) air resides on the right (left) side of
195 the mean wind, which induces a thermal wind in the opposite direction of the mean wind, hence
196 the high angle. For angles around 90° , the relation between the angle and the vertical wind speed
197 gradient is less obvious and we thus only consider the angles $\leq 45^\circ$ and $\geq 135^\circ$ in our study.

198 To test the sensitivity of our results with respect to this strict choice of categories, we also
199 performed our analysis based on a separation at 90° . Similar to Terpstra et al. (2016), we did not
200 find a significant difference in our results, the patterns are only slightly modified, though there is
201 an indication of hybrid PMC types at the separation boundary (not shown).

202 *d. Cyclone track statistics*

203 The mean track duration (distance travelled), plus/minus one standard deviation, is 38.92 ± 24.49
204 h (991 ± 545 km), 39.06 ± 24.71 h (984 ± 533 km), and 38.86 ± 23.47 h (972 ± 505 km) for
205 all, forward, and reverse shear PMCs, respectively (see Fig. 1a). The mean pressure difference
206 between the minimum and genesis pressure along the track is -5.80 ± 7.44 hPa for all PMCs and
207 -7.65 ± 8.50 hPa and -3.15 ± 5.00 hPa for forward and reverse shear PMCs, respectively (Fig.
208 1b). Thus, on average forward shear PMCs deepen more than reverse shear PMCs, though the
209 standard deviations are rather high.

210 For the 850-hPa relative vorticity, the 950-hPa wind, and the difference between the SST and the
211 500-hPa temperature (SST-T500), we have taken the maximum value in a 200-km radius around

212 the cyclone centre for each track point and then considered the maximum value along the track.
 213 The maximum of SST-T500 spans a wide range from 36 to 48 K (41 ± 5 K, see Fig. 1b). The
 214 maximum of relative vorticity covaries with the wind speed (Fig. 1c). The mean maximum vor-
 215 ticity is $1.67 \pm 0.87 \text{ } 10^{-4} \text{ s}^{-1}$, $1.43 \pm 0.78 \text{ } 10^{-4} \text{ s}^{-1}$, $1.73 \pm 0.83 \text{ } 10^{-4} \text{ s}^{-1}$ for all, forward and
 216 reverse shear PMCs, respectively, and the mean maximum wind is $21 \pm 6 \text{ m s}^{-1}$, $19 \pm 6 \text{ m s}^{-1}$, and
 217 $22 \pm 6 \text{ m s}^{-1}$. Therefore, PMCs developing in forward shear conditions tend to be less intense in
 218 terms of relative vorticity and wind speed than PMCs developing in reverse shear conditions. The
 219 mismatch between intensity and pressure deepening suggests that forward shear PMCs include
 220 more weak PMCs than reverse shear PMCs.

221 *e. Rotation of data*

222 As in Terpstra et al. (2016), the atmospheric and surface fields are rotated at the PMC location so
 223 that all PMCs have the same direction of propagation. The angle of rotation is the angle between
 224 geographical north and the direction between the first and the second point of the track. After
 225 rotation, the field is interpolated on a regular grid with resolution $25 \times 25 \text{ km}$. This enables us to
 226 make composites of the synoptic environment of the PMC genesis and mature stages.

227 **3. Climatological aspects of polar mesoscale cyclones**

228 *a. Track densities*

229 We obtain density maps by counting the number of track, genesis, or lysis points in each $0.5^\circ \times$
 230 0.5° grid box, weighting with the area of each grid box, which decreases with increasing latitude,
 231 and smoothing the resulting field $C(\lambda, \varphi)$ with the bell-shaped function

$$d(\lambda, \varphi) = \frac{\sum_{\lambda', \varphi', r < a} F C(\lambda, \varphi)}{\sum_{\lambda', \varphi', r < a} F}, \quad (5)$$

232 with

$$F = \frac{a^2 - r^2}{a^2 + r^2 \left(\frac{a^2}{b^2} - 1 \right)}, \quad (6)$$

233 $a = 250$ km, $b = 100$ km, and the distance r between the considered grid point and the cyclone
234 centre. PMC track positions are counted only once for each grid box to avoid multiple counts
235 of cyclones staying several timesteps in the same grid box. However, the density patterns do not
236 change when counting all track positions and the amplitude is only slightly higher by less than 0.1
237 PMCs per extended winter per 10^4 km 2 .

238 The tracks are mainly over the Norwegian Sea with a maximum west of Svalbard and a sec-
239 ondary maximum between Svalbard and Norway (Fig. 3a), which is in agreement with previous
240 PMC and polar low climatologies (Harold et al. 1999a; Condron et al. 2006; Bracegirdle and Gray
241 2008).

242 PMC genesis occurs close to Svalbard, along the northern Norwegian and Greenland coast, and
243 in the Norwegian Sea (Fig. 3b). These maxima correspond to regions with high occurrence of
244 CAOs (Papritz and Spengler 2017). In addition, Svalbard's topography might play a cyclogenetic
245 role in this area (Bracegirdle and Gray 2008). The Greenland coast also features CAOs, where the
246 position of the sea ice edge or the interaction with orography in the lee of Greenland influences the
247 genesis area (Harold et al. 1999b). The genesis maximum close to Norway is potentially linked to
248 cyclones forming along CAOs predominantly originating from Fram Strait (Papritz and Spengler
249 2017). In contrast to Rojo et al. (2015), the genesis area does not significantly shift eastward
250 during the winter season (not shown). Cyclolysis is rather evenly spread over the domain with a
251 maximum in the Norwegian Sea (Fig. 3c).

252 PMCs forming in forward shear conditions are present over the Norwegian and Barents seas,
253 whereas PMCs forming in reverse shear conditions are much less prevalent over the Barents Sea

254 but occur more often along the Norwegian coast and especially around the Lofoten archipelago
255 (Figs. 3d-i). In addition to genesis maxima west of Svalbard and along Greenland, forward shear
256 genesis also has a maximum west of Novaya Zemlya (Fig. 3e), which is most likely associated with
257 CAOs from the east and the north of the Barents Sea (Papritz and Spengler 2017). By comparing
258 cyclogenesis and lysis densities, we observe that PMCs forming in forward shear conditions have a
259 tendency to move eastward (compare Figs. 3e and f). PMCs developing in reverse shear conditions
260 mainly form in the northern Norwegian Sea and west of Svalbard and tend to travel south towards
261 Norway (compare Figs. 3h and i). The propagation directions and spatial density distribution
262 during forward and reverse shear conditions are in agreement with the STARS database study of
263 Terpstra et al. (2016).

264 *b. Temporal variability*

265 On average, there are 8.00 ± 11.32 PMCs per week per extended winter and 1.87 ± 2.67 ($0.75 \pm$
266 1.09) PMCs per week per extended winter forming in forward (reverse) shear conditions (Fig. 4a).
267 The high standard deviations indicate that there is a large inter-annual variability in the number
268 of PMCs (also found by Harold et al. 1999b; Zahn and von Storch 2008; Rojo et al. 2015). The
269 trend obtained for each of the three time series is 1.3, -2.0, and 0.1 PMCs per extended winter per
270 decade for all, forward, and reverse shear PMCs, respectively. Hence, compared to the standard
271 deviations listed above, we do not observe a significant long term trend in either category, which
272 is consistent with Zahn and von Storch (2008). Even though both forward and reverse shear PMCs
273 can occur at the same time though at different locations (as shown by the cyclogenesis densities,
274 Figs. 3e,h), we observe a slightly negative correlation between PMCs forming in forward and
275 reverse shear conditions (-0.11), which implies that there are fewer reverse shear PMCs when
276 there are more forward shear PMCs and vice versa.

277 The seasonal cycle for all PMCs shows an increase in the number of PMCs per week from Octo-
278 ber to December followed by a decrease until February. A secondary maximum occurs in March
279 followed by a decrease in April (black line on Fig. 4b). PMCs forming in forward and reverse
280 shear conditions have a different seasonal cycle (blue and red lines on Fig. 4b). Forward shear
281 PMCs are most frequent in March whereas reverse shear PMCs are most frequent in February. The
282 minimum in February might be explained by less frequent CAOs during this month, which might
283 be due to relatively higher pressure over Scandinavia during this particular month, as suggested by
284 Noer et al. (2011). Note that the reduced number of days in February has been taken into account
285 by normalising the data by the length of the month.

286 *c. Propagation of polar mesoscale cyclones*

287 As in Terpstra et al. (2016), forward shear PMCs propagate mainly eastward whereas reverse
288 shear PMCs mainly propagate southwestward (Figs. 5a,d), which is in accordance with their
289 synoptic-scale atmospheric flow (Figs. 6a-d). Forward shear PMCs travel slightly faster than
290 reverse shear PMCs with a mean speed of $7.57 \pm 2.38 \text{ m s}^{-1}$ for forward shear PMCs and $6.75 \pm$
291 2.16 m s^{-1} for reverse shear PMCs. These propagation speeds are in agreement with Businger
292 (1985) and Rojo et al. (2015), who also found speeds in the range of $5-13 \text{ m s}^{-1}$. Moreover, Rojo
293 et al. (2015) also mentioned that polar lows can travel in any direction but preferentially south and
294 southeastward.

295 **4. Genesis and mature stage environments**

296 *a. Large-scale genesis environment*

297 To assess the genesis environment, we averaged the 500-hPa geopotential, the potential tempera-
298 ture at the tropopause (Figs. 6a,b), the 850-hPa wind and temperature and the sea ice concentration

299 (Figs. 6c,d) over the genesis dates. Distinguishing between forward and reverse shear genesis con-
300 ditions, it is evident that the two environments feature pronounced differences. At upper levels,
301 forward shear conditions exhibit a ridge both in geopotential and potential temperature (Fig. 6a).
302 At lower levels, there is a southwesterly flow from the North Atlantic towards central Norway,
303 bringing warm air over the Norwegian Sea (Fig. 6c). In addition, there is a weak southward CAO
304 in the Fram Strait diverted towards the Barents Sea.

305 The reverse shear environment features a large trough at upper levels over the Norwegian Sea
306 with an incursion of cold Arctic air (Fig. 6b). At low levels, this trough is linked to a cyclonic
307 circulation centered over the northern Norwegian Sea and a strong CAO along the east Greenland
308 sea ice edge (Fig. 6d). The cyclonic circulation is potentially enhanced by the strong northeastward
309 flow from the North Atlantic towards Northern Europe. The sea ice extent is similar in both
310 environments, except at the northern tip of Novaya Zemlya, suggesting that the sea ice does not
311 play a crucial role in the location of PMC formation. This assertion will be addressed further in
312 section 5.b.

313 *b. Synoptic-scale genesis environment*

314 The rotated fields show similarities compared with the synoptic-scale environments (compare
315 Figs. 6a-d and 7). The forward shear environment features a trough-ridge pattern in 500-hPa
316 geopotential, 850-hPa temperature, and potential temperature on 2-PVU (Potential Vorticity Unit,
317 $10^{-6} \text{ K m}^2 \text{ kg}^{-1} \text{ s}^{-1}$; Fig. 7a). The 850-hPa flow is approximately in the direction of propagation
318 with a weak cyclonic circulation. Moreover, there is a shallow minimum in MSLP with a well-
319 defined warm sector on the right side relative to the direction of propagation, similar to mid-latitude
320 cyclones. The reverse shear environment (Fig. 7b) is characterized by a strong cyclonic circulation
321 (see the MSLP, 850-hPa wind and temperature) with a minimum in potential temperature at 2-PVU

322 above the genesis point. Thus, the characteristics of the reverse shear environment are indicative of
323 an occluded cyclone. From 850-hPa temperature (Fig. 7), it is evident that the highest temperatures
324 are on the right side relative to the direction of propagation in forward shear conditions and on
325 the left side in reverse shear conditions, which is in agreement with the definition of the shear
326 conditions.

327 Figure 8 displays the vertical cross-sections of the wind and potential temperature in the plane
328 perpendicular to the propagation direction at $X = 0$, through the centre of the rotated domain. For
329 forward shear conditions, a jet extends throughout the troposphere with a maximum at 300 hPa in
330 conjunction with a tropopause, i.e, the 2-PVU surface, sloping downward from the right to the left
331 side relative to the direction of propagation (Fig. 8a). In addition, the isentropes show a relatively
332 high horizontal gradient of potential temperature from 1000 to 900 hPa around $Y = 0$, implying
333 that there is a baroclinic zone close to the surface (Fig. 8a). The resemblance of forward shear
334 environments with typical mid-latitude environments suggests the dominance of baroclinic PMC
335 development.

336 Reverse shear conditions show a widening cyclonic circulation from the bottom to the top of the
337 troposphere (Fig. 8b). In addition, there is a strong low-level jet around 925 hPa. These features
338 reflect an occluded extratropical cyclone, which is also evident in Fig. 7b. The tropopause is
339 almost flat with a slight height minimum above the low-level jet (Fig. 8b). The isentropes show
340 a similarly strong baroclinic zone near the surface for both shear conditions, but mid-tropospheric
341 isentropes feature a height minimum at the cyclone centre ($Y = 0$), in contrast to forward shear
342 conditions for which the isentropes are descending on the right-hand-side ($Y < 0$) of the cyclone
343 (compare Figs. 8b and a). This difference is associated with the occluded warm-core cyclone
344 present at genesis time for reverse shear conditions.

345 In the forward shear environment, the surface sensible heat flux is largest to the left side of the
346 cyclone relative to the direction of propagation with a relative minimum over the centre of the
347 cyclone (Fig. 9a). The distribution of the sensible heat fluxes resembles the air-sea temperature
348 difference (SST minus 2-m temperature), except for slightly lower fluxes in the rear-to-right sector
349 due to lower 10-m wind there. SSTs are highest on the rear right side of the cyclone with a
350 minimum on the forward left side (Fig. 9b). The surface latent heat flux is largest in the rear-left
351 sector with higher values surrounding the cyclone, except for the rear-right sector. This structure is
352 similar to the difference between the specific humidity at 2 m and the saturation specific humidity
353 using SST, with relatively higher latent heat flux in the right sector due to higher 10-m wind (Figs.
354 9a,b).

355 In the reverse shear environment, the surface sensible heat flux has a relative minimum over the
356 centre of the cyclone with maximum values on the right-hand-side of the cyclone (Fig. 9c). The
357 minimum in the center is also evident in the air-sea temperature difference as well as the 10-m
358 wind. The maximum in surface sensible heat flux to the right of the cyclone is associated with
359 higher 10-m wind co-located with the low-level jet. Compared to forward shear conditions, SSTs
360 are rather uniform over the area (Fig. 9d). The surface latent heat flux is largest in the rear and to
361 the right of the cyclone. This structure is similar to the difference between the specific humidity
362 at 2 m and the saturation specific humidity using SST, with relatively higher latent heat flux in the
363 right sector due to higher 10-m wind (Figs. 9c,d).

364 The surface fluxes for both forward and reverse shear conditions are thus in accordance with
365 bulk formulas for sensible and latent heat fluxes, which depend on the difference between SST
366 and 2-m temperature and the difference between the specific humidity at 2-m and the saturation
367 specific humidity using SST, respectively, as well as surface wind. Fluxes around the cyclone are
368 significantly higher for reverse shear conditions compared to forward shear conditions, which is

369 related to the higher low-level wind and the presence of a stronger CAO in reverse shear conditions
370 (Figs. 9a,c).

371 The standard deviations of these rotated plots are around 1-3% for all variables with a minimum
372 at the centre of the PMC and increasing radially. A t-test was conducted, with the null hypothesis
373 “Forward shear composite = Reverse shear composite” and assuming that the two composites are
374 independent and normally distributed. This t-test shows that FS and RS composites are statistically
375 different almost everywhere at a significance level of 99% for all variables, except for relative
376 vorticity at 850 hPa, which is only significant on the front side of the cyclone (not shown).

377 *c. Mature stage environment*

378 We define the mature stage as the time for which the MSLP reaches its lowest value during the
379 cyclone lifetime. Another common method is to define the mature stage as the time at which the
380 850-hPa relative vorticity is maximum. In our dataset, 2909 (2678) PMCs have their minimum in
381 pressure occurring after (before) the maximum of vorticity with a time difference of about 16h.
382 2931 PMCs have the minimum in pressure and maximum of vorticity occurring at the same time.
383 Given this relatively symmetric distribution, the choice of vorticity or MSLP to define the mature
384 stage appears not overly significant. Composites of MSLP, relative vorticity at 850 hPa, and wind
385 at 10 m for the mature stage clearly demonstrate that PMCs forming under reverse shear conditions
386 have a higher intensity than PMCs forming in forward shear conditions (Figs. 10a,c).

387 *d. Sensitivity to the SST-T500 parameter*

388 As most previous studies used the temperature difference SST-T500 to distinguish PMCs from
389 polar lows, we analyze the sensitivity of our results to SST-T500, based on SST-T500 at its maxi-
390 mum along the track. We also performed the analysis using SST-T500 at genesis time, but as both

391 criteria basically give the same results we only present the analysis based on the maximum value
392 along the track. We consider three categories: $\text{SST-T500} > 46$ (high values), $40 < \text{SST-T500} < 46$
393 (medium values), and $\text{SST-T500} < 40$ (low values).

394 The percentages of forward shear PMCs satisfying the various conditions of SST-T500 are sim-
395 ilar for all three categories, whereas the percentage of reverse shear PMCs for higher thresholds is
396 greater than for lower thresholds (Table 1). The PMC subset with high SST-T500 contains more
397 polar lows listed in the STARS database than the subset with low SST-T500 (see the percentages
398 in italic in Table 1). Note that some of the STARS polar lows develop in low SST-T500 conditions.

399 For forward shear mesoscale cyclones, the cyclogenesis maximum west of Svalbard (see Fig.
400 3e) can be explained by mesoscale cyclones with high (Fig. 11a) and medium SST-T500 (not
401 shown), contributing with 40% and 60%, respectively. Moreover, up to 80% of the cyclogenesis
402 maximum along the east coast of Greenland is associated with mesoscale cyclones with low SST-
403 T500 (Fig. 11b). The cyclogenesis location of reverse shear mesoscale cyclones remains similar
404 for all categories of SST-T500 (not shown).

405 The direction of propagation for forward shear polar PMCs is related to the choice of the SST-
406 T500 threshold, which is also the case for reverse shear PMCs. PMCs with high SST-T500 prop-
407 agate southeastward in forward shear conditions and south/southwestward in reverse shear condi-
408 tions (Figs. 5b,e), which is in accordance with findings for polar lows (Bracegirdle and Gray 2008;
409 Terpstra et al. 2016). On the other hand, PMCs with low SST-T500 propagate mainly northeast-
410 ward (Figs. 5c,f), contributing to the wider distribution of propagation direction for no SST-T500
411 threshold (Figs. 5a,d).

412 The weak CAO observed in the Fram Strait for the large-scale genesis environment of forward
413 shear PMCs is associated with PMC development during low SST-T500 (compare Figs. 6e and f).

414 For higher SST-T500, there is a strong CAO straight from the Arctic towards Norway (Fig. 6e),

415 rather similar to Fig. 4b of Terpstra et al. (2016). Thus, the lack of significance for the forward
416 shear composite (Fig. 6c) is due to averaging two rather distinct synoptic situations (Figs. 6e,f).

417 In general, the rotated PMC synoptic-scale genesis environment is not strongly influenced by
418 the SST-T500 threshold, as the fields are similar and only their intensity changes. For example,
419 irrespective of the value of SST-T500, reverse shear genesis environments always exhibit a low-
420 level jet and forward shear genesis environments always show a baroclinic zone throughout the
421 entire troposphere with an upper-level jet (not shown), though, as demonstrated in Figs. 6e,f,
422 forward shear conditions contain rather distinct synoptic situations. Moreover, the forward shear
423 genesis environment features a stronger surface baroclinicity for high SST-T500 (not shown), most
424 likely explaining the stronger intensification of these cyclones (see section 2.d). The patterns of
425 the surface heat fluxes of Fig. 9 are dominated by PMCs with low SST-T500, with fluxes being
426 stronger for higher SST-T500 (not shown).

427 In terms of wind and MSLP, reverse shear PMCs are stronger and deeper at their mature stage
428 compared to forward shear PMCs for higher SST-T500 (Figs. 10b,d), with this difference being
429 even more pronounced for low SST-T500 (not shown). When SST-T500 is high, the relative
430 vorticity at 850 hPa is similar at the cyclone centre for forward and reverse shear PMCs, although
431 a bit more spatially spread in the reverse shear conditions (Figs. 10b,d).

432 *e. Intense PMCs*

433 To select intense PMCs at high latitudes, known as polar lows, we applied the following criteria
434 and thresholds: 950-hPa wind speed $> 15 \text{ m s}^{-1}$, SST-T500 > 43 , and 850-hPa relative vorticity
435 $> 6 \cdot 10^{-5} \text{ s}^{-1}$, similar to what is used in previous studies about polar lows (Zahn and von Storch
436 2008; Zappa et al. 2014). To classify a PMC as intense, all criteria have to be fulfilled at the
437 same time, either at the genesis time or the time when they reach their maximum within a radius

438 of 200 km from the cyclone centre. The cyclogenesis density along East Greenland decreases
439 significantly whereas the maxima next to Svalbard and southeast of Iceland are emphasised (not
440 shown) for all, forward and reverse shear conditions. During intense PMCs development, the
441 850-hPa temperature is lower over the Nordic seas, CAOs are stronger, and the surface fluxes
442 are enhanced (not shown). Intense PMCs forming in forward and reverse shear conditions become
443 more similar in strength, as the imposed criteria select the most intense systems (not shown). Thus,
444 the overall characteristics of the genesis environments of intense PMCs are similar to the regular
445 PMCs.

446 **5. Links with atmospheric large-scale variability and Arctic sea ice extent**

447 *a. Large-scale and upper-level atmospheric structure*

448 Compositing the wind at 300 hPa and the 500-hPa geopotential anomaly relative to the winter-
449 time climatology (October to April from 1979 to 2014) for the different shear conditions at genesis
450 time, we obtain geopotential anomaly dipoles that somewhat resemble the two phases of the NAO,
451 where the negative (positive) phase corresponds to forward (reverse) shear conditions (Fig. 12).
452 However, compared to the NAO, the patterns are shifted eastward by about 30° longitude. For for-
453 ward shear conditions, the jet stream has a southwest-northeast orientation and is confined to the
454 western Atlantic. For reverse shear conditions, the jet stream is very strong and extends straight
455 towards the British Isles, Scandinavia, and Russia. The forward (reverse) shear conditions can
456 also be viewed as the positive (negative) phase of SB (defined in the Appendix B), but shifted
457 westward over the Norwegian Sea. Hence, the atmospheric state during forward and reverse shear
458 conditions is neither directly reflecting the NAO nor the SB, but is rather a mix of both. Accord-
459 ingly, the averages during PMC genesis of the daily NAO index (taken from the NOAA Climate

⁴⁶⁰ Prediction Centre³) and SB index (defined in Appendix B) have mean values close to 0 with high
⁴⁶¹ standard deviations. Reverse shear PMC genesis, however, seems to be favoured in the negative
⁴⁶² phase of the SB (see Table 2).

⁴⁶³ Thus, our analysis does not confirm the previously claimed relationship between polar low oc-
⁴⁶⁴ currence and the NAO (Claud et al. 2007). The reasons for this contrast are most likely twofold.
⁴⁶⁵ Firstly, our analysis includes a larger variety of PMCs, thus also mesoscale systems that are not
⁴⁶⁶ polar lows. Secondly, Claud et al. (2007) investigated conditions that are conducive to polar low
⁴⁶⁷ genesis but did not consider genesis based on actual polar low tracks. The latter reasoning is con-
⁴⁶⁸ sistent when comparing our results to Mallet et al. (2013), who come to similar conclusions as
⁴⁶⁹ presented here when using actual polar low tracks. Our finding for reverse shear PMC genesis,
⁴⁷⁰ however, are in accordance with both Claud et al. (2007) and Mallet et al. (2013) featuring higher
⁴⁷¹ occurrence during the negative phase of the SB.

⁴⁷² The mean NAO and SB indices for forward and reverse shear conditions do not have the same
⁴⁷³ sign when considering a less strict angle threshold (e.g., 90°) or for the different SST-T500 cate-
⁴⁷⁴ gories. For high SST-T500, the mean NAO and SB indices for forward and reverse shear PMCs are
⁴⁷⁵ always negative and the standard deviations are halved compared to Table 2 (not shown). These
⁴⁷⁶ mean indices are in accordance with Laffineur et al. (2014), who showed a preference for polar
⁴⁷⁷ low genesis during NAO-, and with Claud et al. (2007) and Mallet et al. (2013), who showed a
⁴⁷⁸ preference for SB-. Given the high sensitivity of these relationships to the chosen thresholds, we
⁴⁷⁹ argue that it is questionable to draw clear conclusions regarding the large-scale environment at
⁴⁸⁰ genesis time.

⁴⁸¹ The negative anomaly in geopotential found over the Norwegian Sea in reverse shear conditions
⁴⁸² (Fig. 12b) is displayed in several polar low climatologies (Businger 1985; Ese et al. 1988; Blech-

³<http://www.cpc.ncep.noaa.gov/products/precip/CWlink/pna/nao.shtml>

483 schmidt et al. 2009; Mallet et al. 2013). This climatological bias is most likely an indication that
 484 the polar lows retained in these studies mainly formed in reverse shear conditions, which could be
 485 related to their criteria chosen for polar low identification.

486 *b. Influence of the Arctic sea ice extent*

487 To investigate the link between the Arctic sea ice extent and the number of PMCs, we define a
 488 standardised index $I(t)$ as

$$I(t) = \frac{A(t) - \bar{A}}{\sigma_A} \quad (7)$$

489 with $A(t)$ the mean sea ice concentration per area for each timestep such as

$$A(t) = \frac{1}{N} \sum_{\lambda, \varphi} sic(\lambda, \varphi, t) a(\lambda, \varphi), \quad (8)$$

490 where λ , φ , and t are longitude, latitude, and time, respectively. N is the number of grid boxes with
 491 area a . sic is the sea ice concentration with values between 0 and 1. The longitude and latitude
 492 span from 20°W to 60°E and from 66°N to 90°N, respectively. The index is standardised by
 493 subtracting its climatological mean over the 35 extended winters (\bar{A}) and dividing by its standard
 494 deviation σ_A .

495 The mean value and standard deviation of the area are $4.74 \pm 0.49 \text{ } 10^9 \text{ km}^2$. Regressing the time
 496 series yields that the mean sea ice extent decrease per decade during the extended winter is -0.28
 497 10^9 km^2 . Hence, the decadal trend is lower than the standard deviation. The cross-correlations
 498 between the mean Arctic sea ice index and the number of PMCs for each extended winter are very
 499 low with -0.16, -0.12, and 0.06 for all PMCs, forward and reverse shear conditions, respectively.

500 To assess the preference of PMC occurrence with respect to sea ice extent, we average the sea
 501 ice index over the genesis dates for all PMCs as well as for both genesis conditions (Table 2). The
 502 mean values are very low with high standard deviations, suggesting that the Arctic sea ice extent

503 does not play a prominent role in modulating the overall occurrence of PMCs. Forward shear
504 conditions tend to be associated with a larger sea ice extent than average, whereas the opposite
505 is true for reverse shear conditions. This could be linked to the seasonal cycle of forward and
506 reverse shear PMC genesis (see Fig. 4), where forward shear PMCs occur more frequently towards
507 the end of the extended winter when the sea ice extent is at its maximum. Furthermore, the
508 decline of sea ice extent in the recent decades mentioned above is not reflected in the time series
509 of PMCs occurring in the area (Fig. 4a). Correlating the detrended index with the number of
510 PMCs during each extended winter also shows negligible negative correlations for any domain
511 and genesis conditions (not shown).

512 Compiling cyclogenesis density for low (high) sea ice extent, i.e., minus (plus) one standard
513 deviation, we find that PMC genesis occurs more frequently close to Norway and in the Norwegian
514 Sea during reduced sea ice extent conditions. On the other hand, genesis is more frequent in the
515 Barents Sea as well as west of Svalbard and along Greenland for increased sea ice extent (Fig.
516 13). Despite these differences in genesis location, the number of PMCs is similar for both sea ice
517 extent conditions. The mean position of the 50% sea ice concentration does not shift much in the
518 western part of the domain compared to the Barents Sea. The lack of correspondence between the
519 sea ice extent and cyclogenesis is also reflected in the fact that the sea ice extent varies significantly
520 throughout the season while the genesis locations of PMCs remains rather unchanged (not shown).

521 With Barents Sea sea ice concentrations projected to decrease significantly for the latter half of
522 the twenty-first century (e.g., Overland and Wang 2007), one might be tempted to speculate about
523 future changes in PMC occurrence based on the track density maps for low sea ice extent (Fig.
524 13a). Of course, using current variability patterns to infer future changes bears significant caveats,
525 but if future changes in sea ice are not accompanied with significant changes in atmospheric and
526 oceanic conditions compared to the present climate, our analysis would indicate that there might be

527 a similar overall number of PMCs in the future with track densities shifted closer to the northern
528 Norwegian coast. This shift would be accompanied with a significant reduction of polar low
529 genesis west of Svalbard and at the same time genesis extending into the ice free areas of the
530 Barents Sea.

531 *c. Association with cold air outbreaks*

532 We test the association of PMC occurrence with CAOs using the percentage of PMCs for which
533 existing CAO criteria are fulfilled for at least one grid point in a radius of 200 km around the
534 cyclone location at least once along the track. We use the CAO indices by Kolstad and Bracegirdle
535 (2008) and Papritz et al. (2015), hereafter referred to as KB and LP, respectively, and the difference
536 between the SST and the temperature at 500 hPa.

537 Table 3 indicates a weak association of CAOs with our detected PMCs. For instance, we obtain
538 only 6.73% for $KB \geq 0.02$ K/hPa, implying that just a few of our detected PMCs occur during a
539 CAO for this threshold. The SST-T500 criterion is the least strict criterion, with 65.33% of our
540 polar mesoscale cyclones forming with $SST-T500 \geq 39$ K, though retaining a larger fraction of
541 reverse shear cyclones than forward shear cyclones.

542 Given these large sensitivities based on different CAO indices and respective thresholds, the
543 appropriateness to use such CAO criteria for polar low detection requires a more detailed assess-
544 ment. Since reverse shear conditions feature larger SST-T500 values than forward shear conditions
545 (Terpstra et al. 2016), one would expect an increased fraction of reverse shear polar lows detected
546 with higher thresholds. However, among the three CAO indices and their respective thresholds,
547 only the SST-T500 index and $KB \geq 0.0$ capture a larger fraction of reverse shear than forward shear
548 PMCs.

549 **6. Concluding remarks**

550 We investigated climatological aspects of PMCs using the Melbourne University cyclone de-
551tection and tracking algorithm over the Nordic seas using the ERA-I reanalysis where we also
552separated PMC genesis environments in forward and reverse shear conditions. The length of our
553dataset is a great advantage compared to previous studies, which allows for a more robust statistical
554analysis, though one caveat of using the ERA-I reanalyses is its representation of mesoscale phe-
555nomena such as polar lows due to its relatively coarse resolution. Laffineur et al. (2014) showed
556that not all polar lows have a MSLP minimum and Zappa et al. (2014) showed that winds associ-
557ated with polar lows are underestimated. Therefore, the robustness of our results should ideally be
558verified using reanalyses with higher resolution, such as the Japanese 55-year Reanalysis (JRA-
559 55, Kobayashi et al. 2015), the Modern-Era Retrospective Analysis for Research and Applications
560 (MERRA, Rienecker et al. 2011), the Arctic System Reanalysis (ASR, Bromwich et al. 2012), or
561the National Centers for Environmental Prediction-Climate Forecast System Reanalysis (NCEP-
562 CFSR, Saha et al. 2010). However, comparing ASR, ERA-I, and polar lows in a 12 km downscaled
563 simulation (Laffineur et al. 2014), Smirnova and Golubkin (2017) suggested that higher resolution
564 data is not necessarily sufficient to give a better representation of polar lows and that the improved
565 representation in ASR is possibly related to the model itself. Thus, whether the improvement
566 in polar low representation is due to model resolution or to the model itself also needs further
567 investigation.

568 Consistent with previous climatologies, we found the highest densities of PMC tracks west of
569 Svalbard as well as between Svalbard and Norway. In addition, we found PMCs occurring along
570 the Greenland sea ice edge and in the Norwegian Sea. PMCs forming in forward shear conditions
571 are present over the entire Nordic seas and propagate mainly eastward, whereas PMCs forming in

572 reverse shear conditions occur more frequently over the Greenland and Norwegian seas and tend
573 to propagate southwestward. The seasonal cycle of PMC occurrence has a peak in January and
574 a slight minimum in February followed by a secondary maximum in March. Forward (reverse)
575 shear PMCs are most frequent in April (January). We find no long-term trend in the number of
576 PMCs for the period 1979-2014, irrespective of the genesis environment conditions in agreement
577 with Zahn and von Storch (2008).

578 In accordance with Terpstra et al. (2016), the temperature gradient near the surface features
579 a baroclinic zone for both shear conditions. For forward shear conditions, the baroclinic zone
580 extends throughout the entire troposphere with a strong jet at 300 hPa on the right side relative to
581 the direction of propagation and a weaker jet around 900 hPa. For reverse shear conditions, there
582 is a quasi-barotropic cyclonic circulation throughout the entire troposphere widening with height
583 as well as a strong and confined low-level jet at 925 hPa.

584 There is a synoptic-scale trough at the tropopause associated with a developing cyclone at low
585 levels with a distinct warm sector for forward shear conditions. For reverse shear conditions, there
586 is a cutoff at the tropopause associated with an occluded cyclone at the surface. PMCs forming in
587 reverse shear conditions become more intense in terms of wind and vorticity during their lifetime
588 than those forming in forward shear conditions. The higher intensity of reverse shear PMCs is
589 in contrast to their lower deepening rates compared to forward shear PMCs. This contrast can be
590 explained by reverse shear PMCs already featuring a lower pressure minimum at genesis time and
591 the subset of forward shear PMCs containing more weak systems.

592 Fluxes are significantly higher for reverse shear PMCs compared to forward shear PMCs, which
593 is mainly due to higher surface wind in reverse shear conditions. Forward shear PMCs tend to
594 have higher SSTs in the rear and to the right side, while reverse shear PMCs propagate through
595 rather uniform SSTs at genesis time.

596 For forward (reverse) shear conditions, there is a ridge (trough) at 500 hPa with warm (cold) air
597 over the Norwegian Sea associated with a mild (strong) CAO over Fram Strait. Thus, our results
598 are in accordance with Terpstra et al. (2016), though the CAO conditions are weaker for forward
599 shear conditions over the Norwegian Sea and the cyclonic circulation centered over Northern Nor-
600 way for reverse shear conditions is weaker and more centered between Svalbard and Norway (Fig.
601 6d). These differences are most likely explained by the fact that Terpstra et al. (2016) is based
602 on the STARS polar low database and, compared to our dataset, they have very few cases in their
603 composites, thereby retaining sharper structures.

604 The 500-hPa geopotential anomalies for PMCs genesis have anomaly dipoles that are neither
605 linked to the NAO nor SB but rather feature a mix of both patterns. Thus, in contrast to Claud
606 et al. (2007), we did not find any significant correlation or association of PMC occurrence with
607 neither the NAO nor SB. However, for reverse shear conditions, we found a preference for the
608 positive (negative) phase of the NAO (SB), consistent with Claud et al. (2007) and Mallet et al.
609 (2013).

610 We constructed an Arctic sea ice extent index over the region from the Greenland Sea to the
611 Barents Sea (between 20°W and 60°E) and found no association with the overall occurrence of
612 PMCs, irrespective of the genesis conditions. However, there is a clear shift in location of PMC
613 occurrence (Fig. 13), with a maximum west of Svalbard in winters with extended sea ice concen-
614 trations and an indication that northern Norway experiences more PMCs during reduced sea ice
615 extent conditions. The cyclogenesis pattern does not seem to be related to the sea ice seasonal
616 cycle and it is likely that other drivers are important, such as the synoptic situation leading to
617 changes in CAO intensity and location.

618 With Barents Sea sea ice concentrations projected to decrease significantly for the latter half of
619 the twenty-first century, our analysis would indicate that there might be a similar overall number

620 of PMCs in the future with track densities shifted closer to the northern Norwegian coast. This
621 shift would be accompanied with a significant reduction of PMC genesis west of Svalbard and a
622 northward migration into ice free areas of the Barents Sea.

623 The association of existing CAO indices with all our detected PMCs is rather weak and the
624 diagnosed co-occurrence is only 5-65% for our PMCs, depending on the strictness of the chosen
625 threshold. The SST-T500 criterion includes more reverse shear PMCs for both chosen thresholds,
626 i.e., $\text{SST-T500} \geq 43 \text{ K}$ and $\text{SST-T500} \geq 39 \text{ K}$, which is probably related to reverse shear genesis
627 environments featuring more statically unstable conditions than forward shear environments. The
628 SST-T500 criterion may be an issue for studies that tried to investigate polar low occurrence in a
629 future climate (e.g., Kolstad and Bracegirdle 2008; Zahn and von Storch 2008), where it is not clear
630 if a potential reduction in reverse shear PMCs might be compensated by an increase in forward
631 shear PMCs. Such a shift in PMC distribution might annihilate or potentially reverse previous
632 results. Considering the potential impact of PMCs on deep convection in the ocean (Condron et al.
633 2008) and CAO erosion (Papritz and Pfahl 2016), it is important to note that although reverse shear
634 PMCs are more intense they are also less frequent. Hence, an assessment of the overall impact of
635 PMCs should include both reverse and forward shear PMCs.

636 *Acknowledgments.* We acknowledge Kevin Keay for his great help with the Melbourne Univer-
637 sity detection and tracking algorithm. We are also grateful to ECMWF for providing the ERA-
638 Interim reanalyses and to the Norwegian Meteorological Institute for the on-line availability of
639 the STARS polar low database. We thank three anonymous reviewers whose useful comments
640 helped to improve this paper. This work is supported by the Norwegian Research Council as
641 part of High Impact Weather in the Arctic (Project 207875) and Marine Cold Air Outbreaks at
642 High Latitudes (Project 262110), and by the European Union's Seventh Framework Programme

643 for research, technological development and demonstration under Marie Curie grant agreement no
644 608695.

645 **APPENDIX A**

646 **Namelist for cyclone detection and tracking**

647 **APPENDIX B**

648 **Scandinavian blocking patterns**

649 The Scandinavian blocking (SB) index is based on the method by Tibaldi and Molteni (1990)
650 using daily 500-hPa geopotential height to detect which longitudes are “blocked”. If half of the
651 longitudes between 0° and 30° E are “blocked”, this timestep is considered to feature a blocking
652 over Scandinavia. The geopotential anomaly relative to the wintertime climatology ($\phi' = \phi - \bar{\phi}$)
653 is then composited for these timesteps to define our Scandinavian blocking pattern (ϕ'_{SB}).

654 Our SB index I is defined using the method of Michel and Rivière (2011) by

$$I(t) = \frac{P(t) - \bar{P}}{\sqrt{\frac{1}{nt} \sum_{t=1}^{nt} [P(t) - \bar{P}]^2}}, \quad (\text{B1})$$

655 where t represents the timestep in the considered period (1 October to 30 April from 1979 to 2014)
656 which contains $nt = 7429$ days. $P(t)$ is the projection of the geopotential anomaly ϕ' on the SB
657 geopotential anomaly ϕ'_{SB}

$$P(t) = \frac{1}{\sum_{(\lambda, \varphi) \in \mathcal{D}} \cos \varphi} \sum_{(\lambda, \varphi) \in \mathcal{D}} \phi'(\lambda, \varphi, t) \phi'_{SB}(\lambda, \varphi) \cos \varphi, \quad (\text{B2})$$

658 where λ and φ are the longitude and latitude, respectively, \mathcal{D} is the domain over which the pro-
659 jection is performed, and \bar{P} is the time mean of the projection over all timesteps. We calculate

660 the index over the North Atlantic – European domain (90°W-60°E/20°N-90°N), but the results are
661 equivalent if the projection is performed over the entire Northern Hemisphere. As both SB phases
662 occur similarly frequent ($\simeq 16\%$), there is no bias that would affect our results.

663 When averaging the days for which the Scandinavian blocking index is higher (lower) than its
664 mean plus (minus) one standard deviation, the structure of the positive (negative) phase is ob-
665 tained. Since we have not found any appropriate figure in the literature, we show the two phases
666 of the Scandinavian blocking on Fig. B1 to help interpret the large-scale structure during polar
667 mesoscale cyclone genesis.

668 **References**

- 669 Blechschmidt, A., 2008: A 2-year climatology of polar low events over the Nordic seas from
670 satellite remote sensing. *Geophys. Res. Lett.*, **35**, L09 815, doi:10.1029/2008GL033706.
- 671 Blechschmidt, A., S. Bakan, and H. Graßl, 2009: Large-scale atmospheric circulation pat-
672 terns during polar low events over the Nordic seas. *J. Geophys. Res.*, D06115, doi:10.1029/
673 2008JD010865.
- 674 Bracegirdle, T. J., and S. L. Gray, 2008: An objective climatology of the dynamical forcing of
675 polar lows in the Nordic seas. *Int. J. Climatol.*, **28**, 1903–1919.
- 676 Bromwich, D., L. Bai, K. Hines, S.-H. Wang, Z. Liu, H.-C. Lin, Y.-H. Kuo, and M. Barlage,
677 2012: Arctic System Reanalysis (ASR) Project. Research Data Archive at the National Center
678 for Atmospheric Research, Computational and Information Systems Laboratory, Boulder CO.
- 679 Businger, S., 1985: The synoptic climatology of polar low outbreaks. *Tellus*, **37A**, 419–432.
- 680 Businger, S., 1987: The synoptic climatology of polar low outbreaks over the Gulf of Alaska and
681 the Bering Sea. *Tellus*, **39A**, 307–325.

- 682 Carrasco, J. F., and D. H. Bromwich, 1992: Mesoscale cyclogenesis over the southeastern Pacific
683 Ocean. *Antarct. J.*, **27**, 289–291.
- 684 Chen, F., and H. von Storch, 2013: Trends and variability of North Pacific polar lows. *Advances*
685 in *Meteorology*, doi:10.1155/2013/170387.
- 686 Claud, C., B. Duchiron, and P. Terray, 2007: Associations between large-scale atmospheric circu-
687 lation and polar low developments over the North Atlantic during winter. *J. Geophys. Res.*, **112**,
688 D12 101, doi:10.1029/2006JD008251.
- 689 Condron, A., G. R. Bigg, and I. A. Renfrew, 2006: Polar mesoscale cyclones in the Northeast
690 Atlantic: Comparing climatologies from ERA-40 and satellite imagery. *Mon. Wea. Rev.*, **134**,
691 1518–1533.
- 692 Condron, A., G. R. Bigg, and I. A. Renfrew, 2008: Modeling the impact of polar mesocyclones on
693 ocean circulation. *J. Geophys. Res.*, **113**, 17 pp.
- 694 Condron, A., and I. A. Renfrew, 2013: The impact of polar mesoscale storms on northeast Atlantic
695 Ocean circulation. *Nature*, **6**, 34–37.
- 696 Dee, D., and Coauthors, 2011: The ERA-Interim reanalysis: configuration and performance of the
697 data assimilation system. *Quart. J. Roy. Meteor. Soc.*, **137**, 553–597.
- 698 Duncan, C., 1978: Baroclinic instability in a reversed shear flow. *Meteor. Mag.*, **107**, 17–23.
- 699 Ese, T., I. K. m, and K. Pedersen, 1988: Climatology of polar lows over the Norwegian and Barents
700 Seas. *Tellus*, **40A**, 248–255.
- 701 Forbes, G. S., and W. D. Lottes, 1985: Classification of mesoscale vortices in polar airstreams and
702 the influence of the large-scale environment on their evolutions. *Tellus*, **37A**, 132–155.

- 703 Harold, J. M., G. R. Bigg, and J. Turner, 1999a: Mesoscale activity over the North-East Atlantic.
- 704 Part 1: Vortex distribution and variability. *Int. J. Climatol.*, **19**, 1187–1204.
- 705 Harold, J. M., G. R. Bigg, and J. Turner, 1999b: Mesoscale activity over the North-East Atlantic.
- 706 Part 2: An investigation of causal mechanisms. *Int. J. Climatol.*, **19**, 1283–1299.
- 707 Irving, D., I. Simmonds, and K. Keay, 2010: Mesoscale cyclone activity over the ice-free Southern
- 708 Ocean: 1999–2008. *J. Climate*, **23**, 5404–5420.
- 709 Kobayashi, S., and Coauthors, 2015: The JRA-55 Reanalysis: General specifications and basic
- 710 characteristics. *J. Meteor. Soc. Japan*, **93**, 5–48.
- 711 Kolstad, E. W., 2006: A new climatology of favourable conditions for reverse-shear polar lows.
- 712 *Tellus*, **58A**, 344–354.
- 713 Kolstad, E. W., and T. J. Bracegirdle, 2008: Marine cold-air outbreaks in the future: an assessment
- 714 of IPCC AR4 model results for the Northern hemisphere. *Climate Dyn.*, **30**, 871–885.
- 715 Kolstad, E. W., T. J. Bracegirdle, and I. A. Seierstad, 2009: Marine cold-air outbreaks in the
- 716 North Atlantic: temporal distribution and associations with large-scale atmospheric circulation.
- 717 *Climate Dyn.*, **22**, 187–197.
- 718 Laffineur, T., C. Claud, J.-P. Chaboureau, and G. Noer, 2014: Polar lows over the Nordic Seas:
- 719 Improved representation in ERA-Interim compared to ERA-40 and the impact on downscaled
- 720 simulations. *Mon. Wea. Rev.*, **142**, 2271–2289.
- 721 Mallet, P.-E., C. Claud, C. Cassou, G. Noer, and K. Kodera, 2013: Polar lows over the Nordic
- 722 and Labrador Seas: Synoptic circulation patterns and associations with North Atlantic-Europe
- 723 wintertime weather regimes. *J. Geophys. Res.*, **118**, 2455–2472.

- 724 Michel, C., and G. Rivière, 2011: The link between Rossby wave breakings and weather regime
725 transitions. *J. Atmos. Sci.*, **68**, 1730–1748.
- 726 Mokhov, I., M. Akperov, V. Lagun, and E. Lutsenko, 2007: Intense Arctic mesocyclones. *Atm.*
727 *and Ocean. Phys.*, **43**, 259–265.
- 728 Moore, G. W. K., I. A. Renfrew, B. E. Harden, and S. H. Mernild, 2015: The impact of resolution
729 on the representation of southeast Greenland barrier winds and katabatic flows. *Geophys. Res.*
730 *Lett.*, **42**, 3011–3018.
- 731 Murray, R. J., and I. Simmonds, 1991a: A numerical scheme for tracking cyclone centres from
732 digital data. Part I: development and operation of the scheme. *Aust. Met. Mag.*, **39**, 155–166.
- 733 Murray, R. J., and I. Simmonds, 1991b: A numerical scheme for tracking cyclone centres from
734 digital data. Part II: application to January and July general circulation model simulations. *Aust.*
735 *Met. Mag.*, **39**, 167–180.
- 736 Noer, G., Ø. Saetra, T. Lien, and Y. Gusdal, 2011: A climatological study of polar lows in the
737 Nordic Seas. *Quart. J. Roy. Meteor. Soc.*, **137**, 1762–1772, doi:10.1002/qj.846.
- 738 Overland, J. E., and M. Wang, 2007: Future regional Arctic sea ice declines. *Geophys. Res. Lett.*,
739 **34**, doi:10.1029/2007GL030808.
- 740 Papritz, L., and S. Pfahl, 2016: Importance of latent heating in mesocyclones for the decay of cold
741 air outbreaks: A numerical process study from the Pacific sector of the Southern Ocean. *Mon.*
742 *Wea. Rev.*, **144**, 315–336.
- 743 Papritz, L., S. Pfahl, H. Sodemann, and H. Wernli, 2015: A climatology of cold air outbreaks and
744 their impact on air-sea heat fluxes in the high-latitude South Pacific. *J. Climate*, **28**, 342–364.

- 745 Papritz, L., and T. Spengler, 2017: A Lagrangian climatology of wintertime cold air outbreaks
746 in the Irminger and Nordic seas and their role in shaping air-sea heat fluxes. *J. Climate*, **30**,
747 2717–2737.
- 748 Rasmussen, E. A., and J. Turner, 2003: *Polar lows: mesoscale weather systems in the polar*
749 *regions*. Cambridge University Press, New York, 612 pp.
- 750 Rienecker, M. M., and Coauthors, 2011: MERRA: NASA’s Modern Era Retrospective Analysis
751 for research and applications. *J. Climate*, **24**, 3624–3648.
- 752 Rojo, M., C. Claud, P.-E. Mallet, G. Noer, A. M. Carleton, and M. Vicomte, 2015: Po-
753 lar low tracks over the Nordic Seas: a 14-winter climatic analysis. *Tellus*, **67A**, 24 660,
754 <http://dx.doi.org/10.3402/tellusa.v67.24660>.
- 755 Sætra, Ø., Y. Gusdal, S. Eastwood, J. Debernard, P.-E. Isachesen, H. Schyberg, B. Furevik, and
756 G. Noer, 2010: Scientific analysis plan (d3). Tech. rep., Norwegian Meteorological Institute.
- 757 Saha, S., and Coauthors, 2010: The NCEP Climate Forecast System Reanalysis. *Bull. Amer. Me-*
758 *teor. Soc.*, **91**, 1015–1057.
- 759 Smirnova, J., and P. Golubkin, 2017: Comparing polar lows in atmospheric reanalyses: Arctic
760 System Reanalysis versus ERA-Interim. *Mon. Wea. Rev.*, accepted.
- 761 Terpstra, A., C. Michel, and T. Spengler, 2016: Forward and reverse shear environments during
762 polar low genesis over the Northeast Atlantic. *Mon. Wea. Rev.*, **144**, 1341–1354.
- 763 Tibaldi, S., and F. Molteni, 1990: On the operational predictability of blocking. *Tellus*, **42A**, 343–
764 365.

- 765 Turner, J., and J. P. Thomas, 1994: Summer-season mesoscale cyclones in the Bellingshausen-
766 Weddell region of the Antarctic and links with the synoptic-scale environment. *Int. J. Climatol.*,
767 871–894.
- 768 Uppala, S. M., and Coauthors, 2005: The ERA-40 re-analysis. *Quart. J. Roy. Meteor. Soc.*, **131**,
769 2961–3012.
- 770 Wilhelmsen, K., 1985: Climatological study of gale-producing polar lows near Norway. *Tellus*,
771 **37A**, 451–459.
- 772 Yanase, W., H. Niino, S.-I. I. Watanabe, K. Hodges, M. Zahn, T. Spengler, and I. A. Gervich, 2016:
773 Climatology of polar lows over the Sea of Japan using the JRA-55 Reanalysis. *J. Climate*, **29**,
774 419–437.
- 775 Yarnal, B., and K. G. Henderson, 1989: A satellite-derived climatology of polar low evolution in
776 the North Pacific. *Int. J. Climatol.*, **9**, 551–566.
- 777 Zahn, M., and H. von Storch, 2008: A long-term climatology of North Atlantic polar lows. *Geo-
778 phys. Res. Lett.*, **35**, L22 702, doi:10.1029/2008GL035769.
- 779 Zappa, G., L. Shaffrey, and K. Hodges, 2014: Can polar lows be objectively identified and tracked
780 in the ECMWF operational analysis and the ERA-Interim reanalysis? *Mon. Wea. Rev.*, **142**,
781 2596–2608.

782 LIST OF TABLES

783	Table 1. Number of tracks of PMCs with no SST-T500 threshold (first row) and de-	pending on the SST-T500 maximum in a 200-km radius at its maximum along the track [Max(SST-T500)] or at the genesis time [Gen(SST-T500)]. The per-	37
784	centages in italic in column ALL show the percentages of tracks matching the		
785	tracks of the STARS database. The percentages in columns FS and RS show		
786	the percentages of FS and RS tracks relatively to the total number of tracks		
787	given in column ALL.		
788			
789			
790	Table 2. North Atlantic Oscillation (NAO), Scandinavian Blocking (SB), Arctic Sea Ice		
791	Extent (ASIE) indices averaged over the genesis dates for PMCs along with		
792	their standard deviations for all polar mesoscale cyclones (ALL) and the PMCs		
793	formed in forward (FS) and reverse shear (RS) conditions.		
794	Table 3. Percentage of PMCs for which the respective CAO criterion is fulfilled for at		
795	least one grid point in a 200-km radius around the cyclone center at least once		
796	along the track. LP and KB refer to Papritz et al. (2015) and Kolstad and Brace-		
797	girdle (2008), respectively, with the indicated thresholds. SST-T500 refers to		
798	the difference between the SST and the temperature at 500 hPa. ALL, FS, and		
799	RS, refer to all, forward, and reverse shear PMCs, respectively. Units are K for		
800	LP and SST-T500, and K/hPa for KB.		
801	Table A1. Values of the parameters for the detection and tracking namelists used by the		
802	algorithm.		
803			
804			
805			
806			
807			
808			
809			
810			
811			
812			
813			
814			
815			
816			
817			
818			
819			
820			
821			
822			
823			
824			
825			
826			
827			
828			
829			
830			
831			
832			
833			
834			
835			
836			
837			
838			
839			
840			
841			
842			
843			
844			
845			
846			
847			
848			
849			
850			
851			
852			
853			
854			
855			
856			
857			
858			
859			
860			
861			
862			
863			
864			
865			
866			
867			
868			
869			
870			
871			
872			
873			
874			
875			
876			
877			
878			
879			
880			
881			
882			
883			
884			
885			
886			
887			
888			
889			
890			
891			
892			
893			
894			
895			
896			
897			
898			
899			
900			
901			
902			
903			
904			
905			
906			
907			
908			
909			
910			
911			
912			
913			
914			
915			
916			
917			
918			
919			
920			
921			
922			
923			
924			
925			
926			
927			
928			
929			
930			
931			
932			
933			
934			
935			
936			
937			
938			
939			
940			
941			
942			
943			
944			
945			
946			
947			
948			
949			
950			
951			
952			
953			
954			
955			
956			
957			
958			
959			
960			
961			
962			
963			
964			
965			
966			
967			
968			
969			
970			
971			
972			
973			
974			
975			
976			
977			
978			
979			
980			
981			
982			
983			
984			
985			
986			
987			
988			
989			
990			
991			
992			
993			
994			
995			
996			
997			
998			
999			
9999			

803 TABLE 1. Number of tracks of PMCs with no SST-T500 threshold (first row) and depending on the SST-
 804 T500 maximum in a 200-km radius at its maximum along the track [Max(SST-T500)] or at the genesis time
 805 [Gen(SST-T500)]. The percentages in italic in column ALL show the percentages of tracks matching the tracks
 806 of the STARS database. The percentages in columns FS and RS show the percentages of FS and RS tracks
 807 relatively to the total number of tracks given in column ALL.

	ALL	FS	RS
No threshold	8518	2002 (23.5%)	800 (9.4%)
Max(SST-T500)>46	1461 (<i>49%</i>)	354 (24.2%)	210 (14.4%)
40<Max(SST-T500)<46	3482 (<i>11%</i>)	793 (22.8%)	388 (11.1%)
Max(SST-T500)<40	3575 (<i>0.7%</i>)	855 (22.8%)	202 (5.7%)
Gen(SST-T500)>46	633 (<i>31%</i>)	150 (23.7%)	92 (14.5%)
40<Gen(SST-T500)<46	2466 (<i>20%</i>)	566 (23.0%)	311 (12.6%)
Gen(SST-T500)<40	5419 (<i>12%</i>)	1286 (23.7%)	397 (7.3%)

808 TABLE 2. North Atlantic Oscillation (NAO), Scandinavian Blocking (SB), Arctic Sea Ice Extent (ASIE)
 809 indices averaged over the genesis dates for PMCs along with their standard deviations for all polar mesoscale
 810 cyclones (ALL) and the PMCs formed in forward (FS) and reverse shear (RS) conditions.

	ALL	FS	RS
NAO	0.167 ± 0.806	-0.007 ± 0.777	0.227 ± 0.859
SB	-0.004 ± 0.968	0.180 ± 0.960	-0.441 ± 0.945
ASIE	0.018 ± 0.985	0.087 ± 0.981	-0.013 ± 0.953

811 TABLE 3. Percentage of PMCs for which the respective CAO criterion is fulfilled for at least one grid point
 812 in a 200-km radius around the cyclone center at least once along the track. LP and KB refer to Papritz et al.
 813 (2015) and Kolstad and Bracegirdle (2008), respectively, with the indicated thresholds. SST-T500 refers to the
 814 difference between the SST and the temperature at 500 hPa. ALL, FS, and RS, refer to all, forward, and reverse
 815 shear PMCs, respectively. Units are K for LP and SST-T500, and K/hPa for KB.

	All (8518)	FS (2002)	RS (800)
LP \geq 4	50.74%	60.04%	56.88%
LP \geq 6	35.14%	46.1%	36.63%
KB \geq 0	33.87%	40.36%	43%
KB \geq 0.01	17.41%	23.78%	18.75%
KB \geq 0.02	6.73%	10.49%	5.38%
SST-T500 \geq 39	65.33%	63.54%	81%
SST-T500 \geq 43	35.94%	35.91%	50%

Table A1. Values of the parameters for the detection and tracking namelists used by the algorithm.

Cyclone detection							
ni = nj	721	drmx1	0.7	fccmn	0.0	upfact	1.0
rproj	360	drmx2	0.3	cvarad	1.25	zsmax	1000
rdiff	0.3	itm1 = itm2	10	nrrdir	18	zscr1	200
rdifz	0.0	diflt1 = diflt2	2.0	rdincr	0.5	zscr2	1000
iopmxc	1	cmnh = cmnc	0.0	sphtrg	.false.	ftopeq	0.01
istmxc	11	cmnc1	0.2	rdpgrd	5.0	cmncw	1.0
nshell	8	cmnc2	0.5	npgdir	12	dpmnw	-999
mscrn	2	dpmn	0.1	alatgv	8.0	swvmnw	0.0
sdrmx	10	swvmn	1.0	rhoa	1.2	-	-
Tracking							
refdt	0.25	dequiv	0.0	rpbell	0.4	pstrak	.false.
wsteer	0.4	wpten	0.8	qmxopn	0.6	irevmx	400
fsteer	2.25	wmotn	1.0	qmxwek	0.6	-	-
asteer	0.0	rcprob	8.0	qmxnew	0.6	-	-

816 LIST OF FIGURES

- 817 **Fig. 1.** Two-dimensional histograms of (a) distance traveled by the cyclone (unit: km) as a function
 818 of the cyclone lifetime (unit: hours), (b) maximum 850-hPa relative vorticity (unit: 10^{-4}
 819 s^{-1}) as a function of the maximum difference between the SST and the 500-hPa temperature
 820 reached during the cyclone lifetime (unit: K), and (c) maximum 850-hPa relative vorticity
 821 (unit: $10^{-4} s^{-1}$) as a function of the maximum 950-hPa wind (unit: $m s^{-1}$) reached during
 822 the cyclone lifetime. All maximum values for (b) and (c) are taken in a 200-km radius
 823 around the cyclone centre. 43
- 824 **Fig. 2.** Vertical wind speed gradient between 700 and 925 hPa (unit: $10^{-3} s^{-1}$) as a function of
 825 the angle (α) between the thermal and the mean wind (unit: degrees) for all PMCs at their
 826 genesis time. The vertical gradient and the angle have been averaged in a 200-km radius
 827 around the genesis location. The purple lines represent $\alpha = 45^\circ$ and $\alpha = 135^\circ$ which are the
 828 limits defining forward and reverse shear conditions, respectively. 44
- 829 **Fig. 3.** (a,d,g) Track densities, (b,e,h) cyclogenesis densities, and (c,f,i) lysis densities for (a-c) all
 830 PMCs, (d-f) PMCs formed in forward shear (FS) conditions, and (g-i) in reverse shear
 831 (RS) conditions. Unit is number of PMCs per extended winter per 10^4 km^2 . Note the
 832 difference in the colorbars. 45
- 833 **Fig. 4.** (a) Number of PMCs per extended winters and (b) per month. The black line corresponds
 834 to all PMCs (ALL). The blue (red) lines correspond to PMCs formed in forward (reverse)
 835 shear conditions (FS, RS). (b) The dashed lines show +/- one standard deviation around each
 836 point. 46
- 837 **Fig. 5.** Propagation direction frequency (length of the pieces) along with the propagation speed
 838 (shading, unit: $m s^{-1}$) for (a-c) PMCs developing during forward shear (FS) conditions and
 839 (d-f) in reverse shear (RS) conditions. In (a,d), no threshold in SST-T500 is applied to select
 840 the tracks. For (b,e) (c,f), only the tracks for which $\text{Max}(\text{SST-T500}) > 46$ (< 40) are used.
 841 $\text{Max}(\text{SST-T500})$ is defined in the text. 47
- 842 **Fig. 6.** (a,b) Geopotential at 500-hPa (black contours, interval: $500 \text{ m}^2 \text{ s}^{-2}$) and potential temperature
 843 at the tropopause defined by the 2-PVU surface (shading, unit: K) averaged over the
 844 genesis dates of PMCs. (c-f) Temperature at 850 hPa (shading, unit: K), wind at 850 hPa
 845 (arrows), and sea ice concentration (black line corresponding to a value of 0.5) averaged
 846 over the genesis dates of PMCs. (a,c) Fields averaged for PMCs formed in forward shear
 847 (FS) conditions and (b,d) reverse shear (RS) conditions. (e) (f) Fields averaged for PMCs
 848 formed in FS conditions and having $\text{Max}(\text{SST-T500}) > 46$ (< 40). The solid (dashed) blue
 849 lines represent the 99% (95%) confidence levels calculated using a bootstrap method with
 850 (a,b) the 500-hPa geopotential and (c-f) the 850-hPa temperature. 48
- 851 **Fig. 7.** Composites of potential temperature at 850 hPa (shading, unit: K), wind at 850 hPa (arrows),
 852 geopotential at 500 hPa (dashed blue contours, interval: $200 \text{ m}^2 \text{ s}^{-2}$), potential temperature
 853 at 2 PVU (black contours, interval: 2 K), and mean sea level pressure (white contours,
 854 interval: 2 hPa) for the genesis time of (a) PMCs forming in forward shear (FS) conditions
 855 and (b) in reverse shear (RS) conditions. The direction propagation is towards increasing X
 856 values. 49
- 857 **Fig. 8.** Cross-sections in the direction of propagation of the wind (shading, unit: $m s^{-1}$), potential
 858 temperature (black contours, interval: 5 K), and the tropopause defined as the 2-PVU surface
 859 (blue line) composited for the genesis times of (a) PMCs formed in forward shear (FS)
 860 conditions, and (b) in reverse shear (RS) conditions. The positive (negative) values of Y

represent the left (right) side relative to the propagation direction which is directed into the page.

50

Fig. 9. Composites of sensible (a,c) and latent (b,d) heat fluxes (shading, unit: W m^{-2}) for genesis time of PMCs during (a,b) forward shear (FS) conditions and (c,d) reverse shear (RS) conditions. Overlaid are (a,c) difference between SST and 2-m temperature (solid lines, unit: K) together with 10-m wind (arrows) and (b,d) SST (white solid contours, unit: K) together with the difference between specific humidity at 2 m and saturation specific humidity using SST (dashed contours, unit: g kg^{-1}). Values over 50% sea ice concentration or over land are omitted in the composites and areas are shaded where this omission occurs in more than half of the PMC cases. The direction of propagation is towards increasing X values. A nine-point local smoothing is applied to the fields after compositing.

51

Fig. 10. Composites of the 10-m wind speed (shading, unit: m s^{-1}), mean sea level pressure (solid black contours, interval: 5 hPa), and relative vorticity at 850 hPa (dashed black contours, unit: 10^{-6} s^{-1} , interval: $20 \cdot 10^{-6} \text{ s}^{-1}$) for the mature stage of PMCs formed in (a,c) forward shear (FS) conditions and (b,d) reverse shear (RS) conditions. For (a,c) no threshold in SST-T500 is applied to the tracks. For (b,d) only tracks with $\text{Max}(\text{SST-T500}) > 46$ are used. The propagation direction is towards increasing X values. The mature stage is defined as the time for which the mean sea level pressure reaches its lowest value during the cyclone lifetime.

52

Fig. 11. Cyclogenesis densities for PMCs forming in forward shear conditions and having (a) $\text{Max}(\text{SST-T500}) > 46$ and (b) $\text{Max}(\text{SST-T500}) < 40$. Unit is a number of polar lows per extended winter per 10^4 km^2 .

53

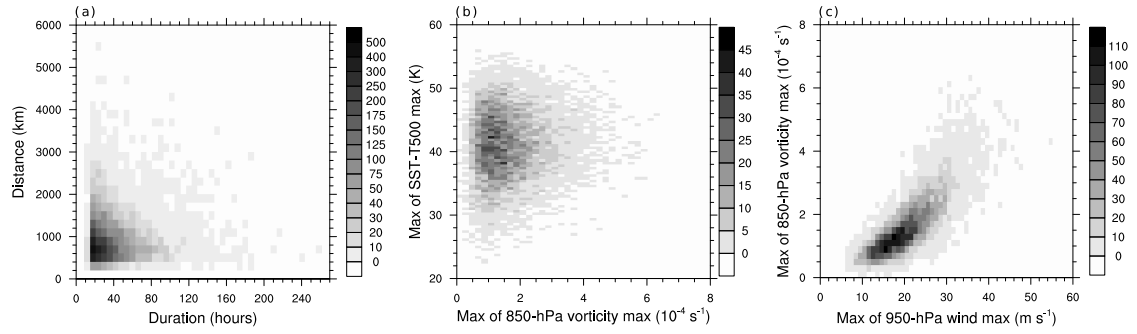
54

Fig. 13. Cyclogenesis density of PMCs for the Arctic sea ice extent index (a) (b) lower (greater) than its mean minus (plus) one standard deviation. Unit is number of PMCs per extended winter per 10^4 km 2 . The red line represents 50% sea ice concentration.

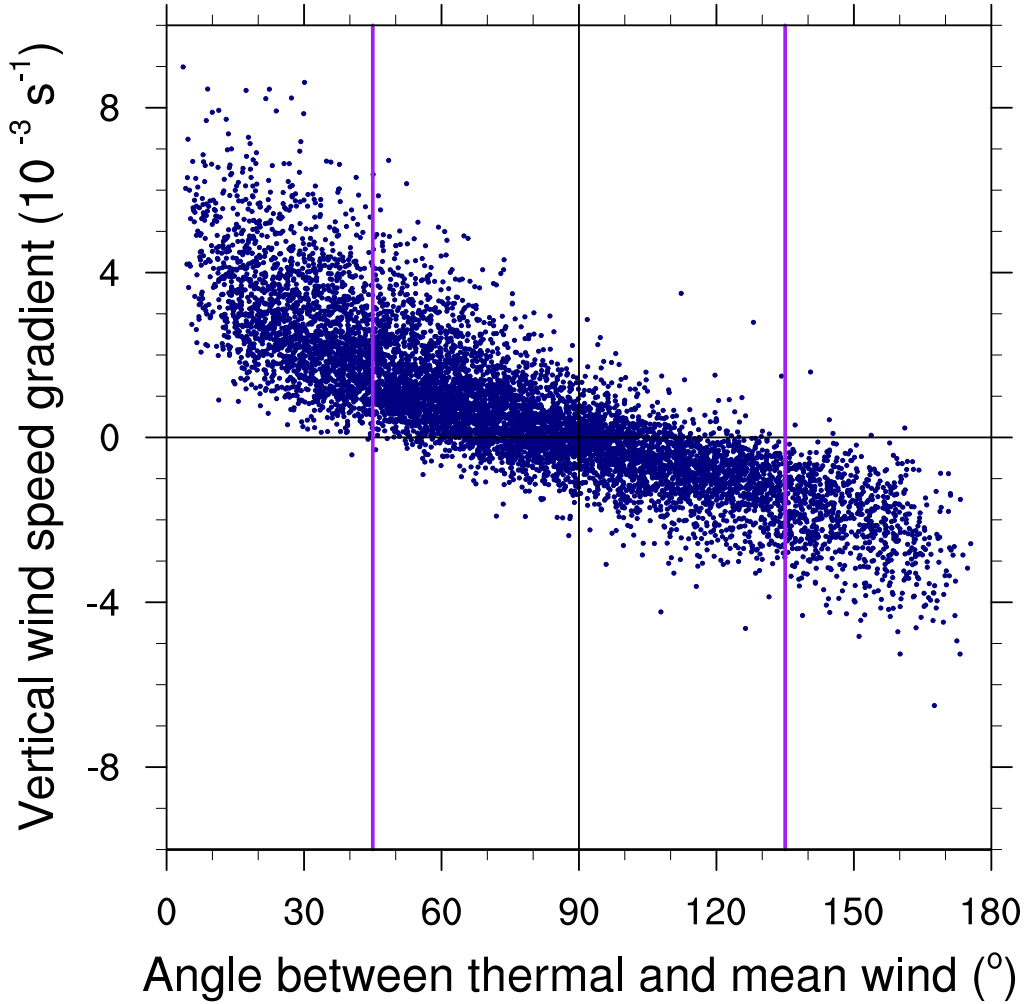
55

Fig. B1. Composites of the (a) positive and (b) negative phases of the Scandinavian Blocking of the 500-hPa geopotential (shading, unit: dam), 10-m wind (arrows) and the 50% sea ice concentration contour (red line) for the period 1979-2014. The positive (negative) phases are defined as the days for which the index is higher (lower) than the mean plus (minus) one standard deviation.

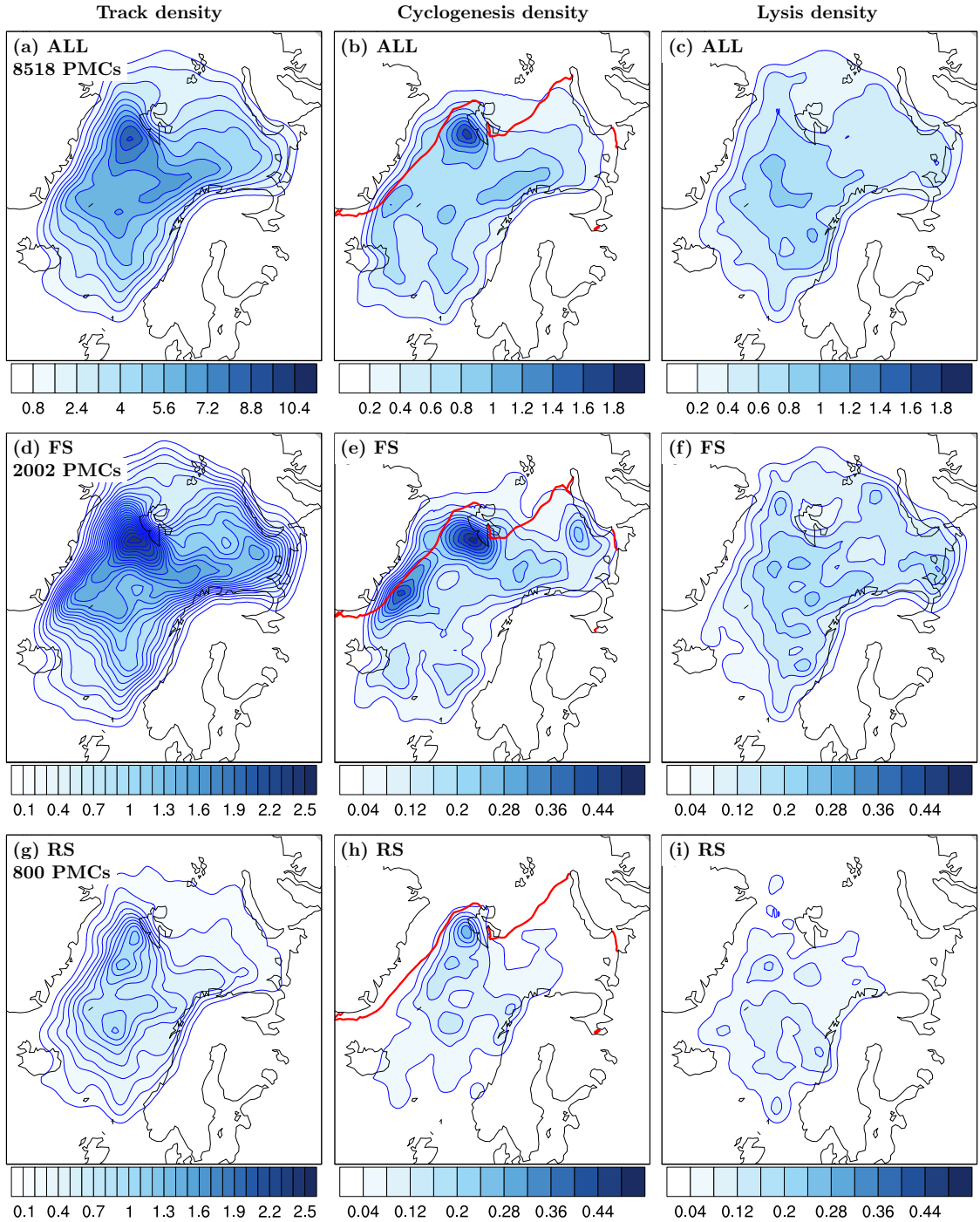
56



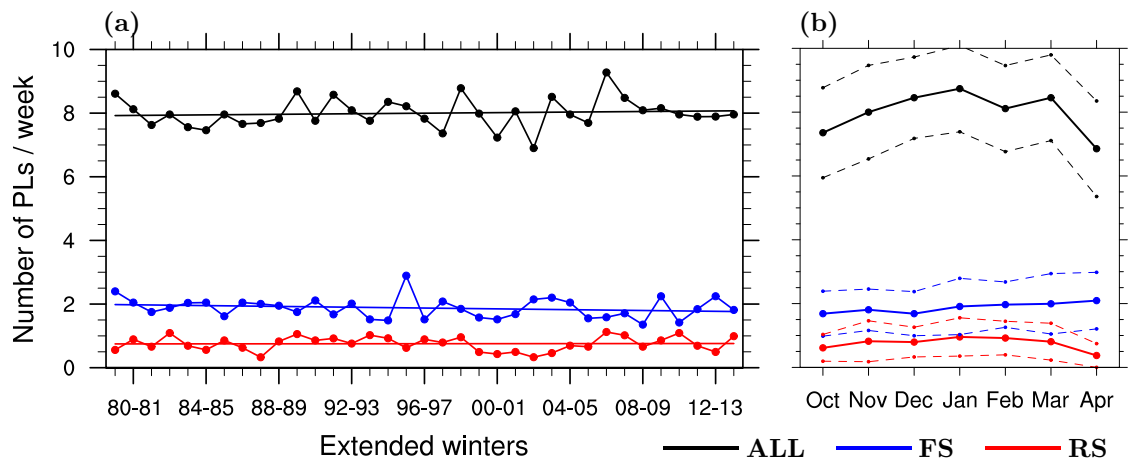
894 FIG. 1. Two-dimensional histograms of (a) distance traveled by the cyclone (unit: km) as a function of the
 895 cyclone lifetime (unit: hours), (b) maximum 850-hPa relative vorticity (unit: 10^{-4} s^{-1}) as a function of the
 896 maximum difference between the SST and the 500-hPa temperature reached during the cyclone lifetime (unit:
 897 K), and (c) maximum 850-hPa relative vorticity (unit: 10^{-4} s^{-1}) as a function of the maximum 950-hPa wind
 898 (unit: m s^{-1}) reached during the cyclone lifetime. All maximum values for (b) and (c) are taken in a 200-km
 899 radius around the cyclone centre.



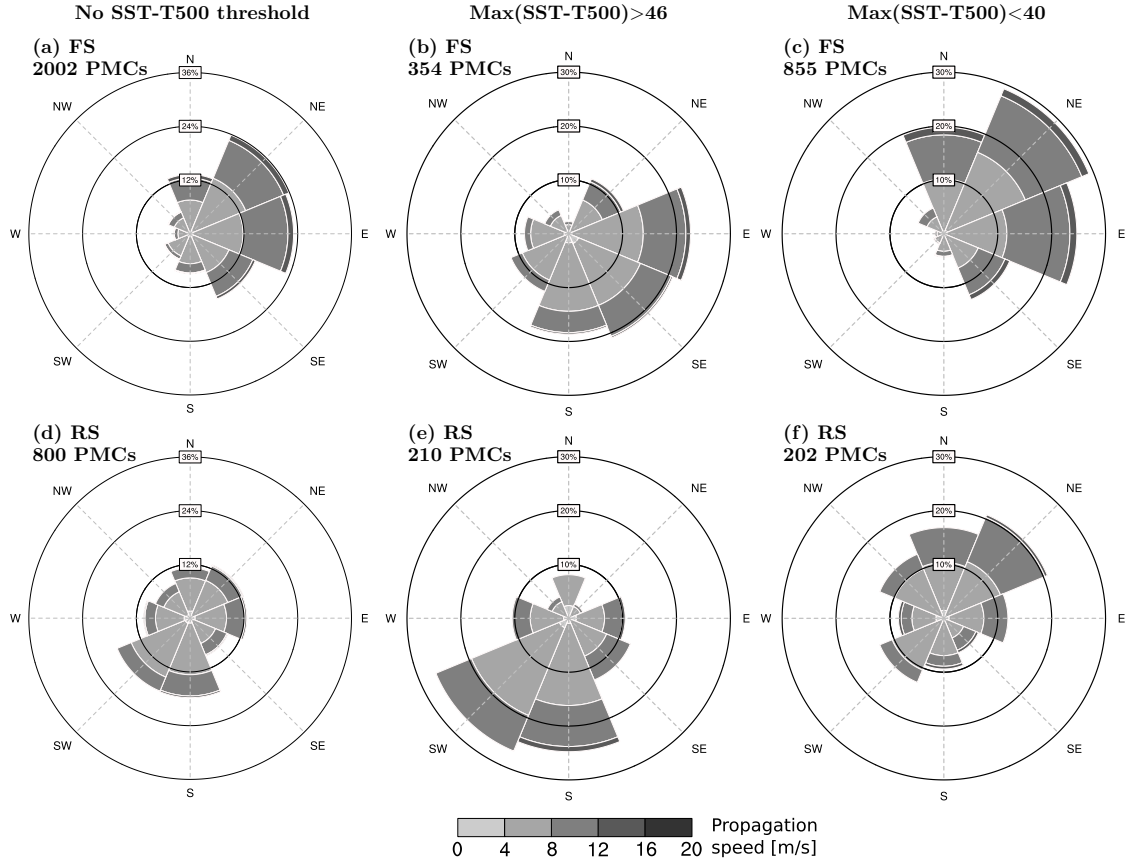
900 FIG. 2. Vertical wind speed gradient between 700 and 925 hPa (unit: 10^{-3} s^{-1}) as a function of the angle (α)
 901 between the thermal and the mean wind (unit: degrees) for all PMCs at their genesis time. The vertical gradient
 902 and the angle have been averaged in a 200-km radius around the genesis location. The purple lines represent
 903 $\alpha = 45^{\circ}$ and $\alpha = 135^{\circ}$ which are the limits defining forward and reverse shear conditions, respectively.



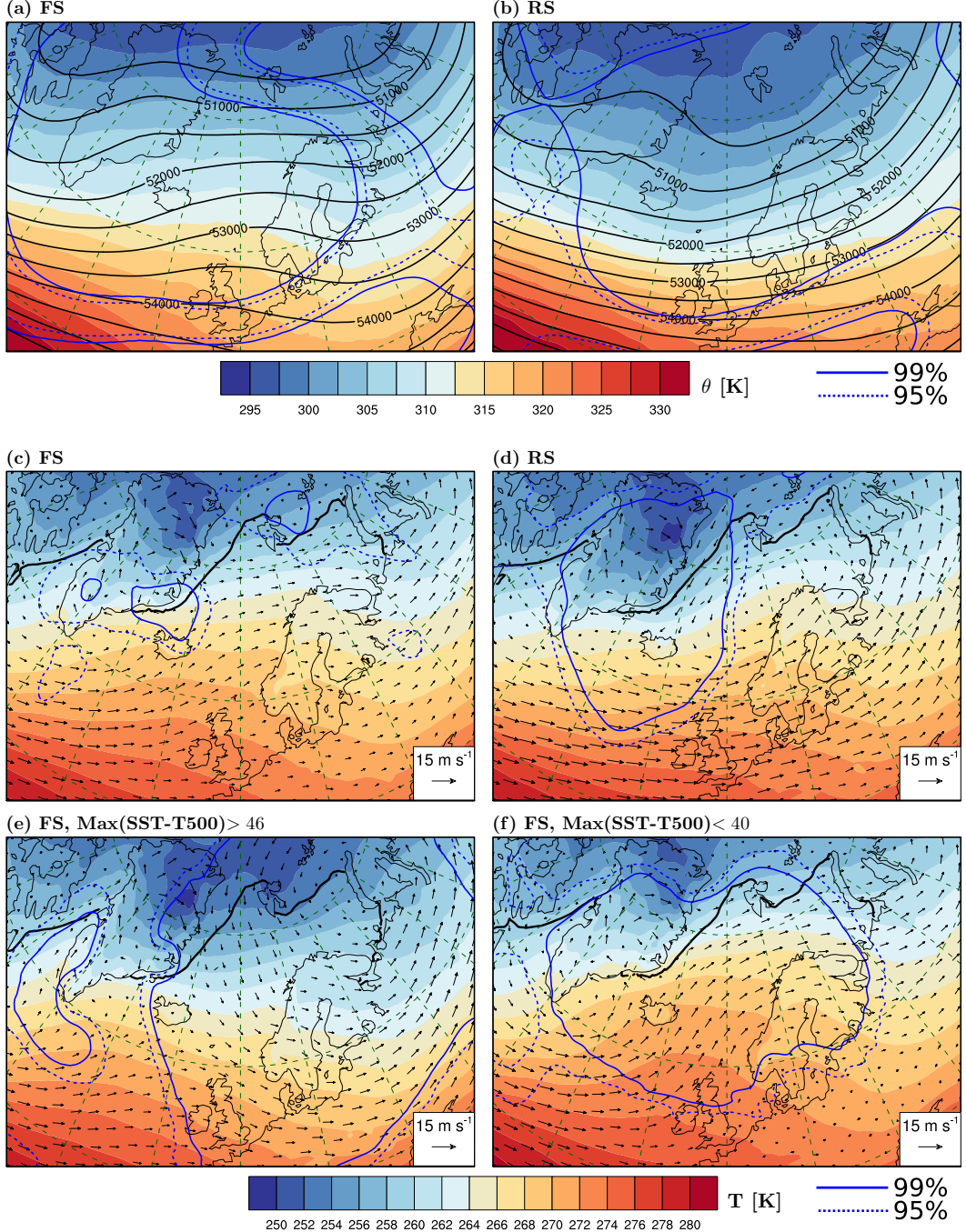
904 FIG. 3. (a,d,g) Track densities, (b,e,h) cyclogenesis densities, and (c,f,i) lysis densities for (a-c) all PMC
 905 tracks, (d-f) PMCs formed in forward shear (FS) conditions, and (g-i) in reverse shear (RS) conditions. Unit is
 906 number of PMCs per extended winter per 10^4 km^2 . Note the difference in the colorbars.



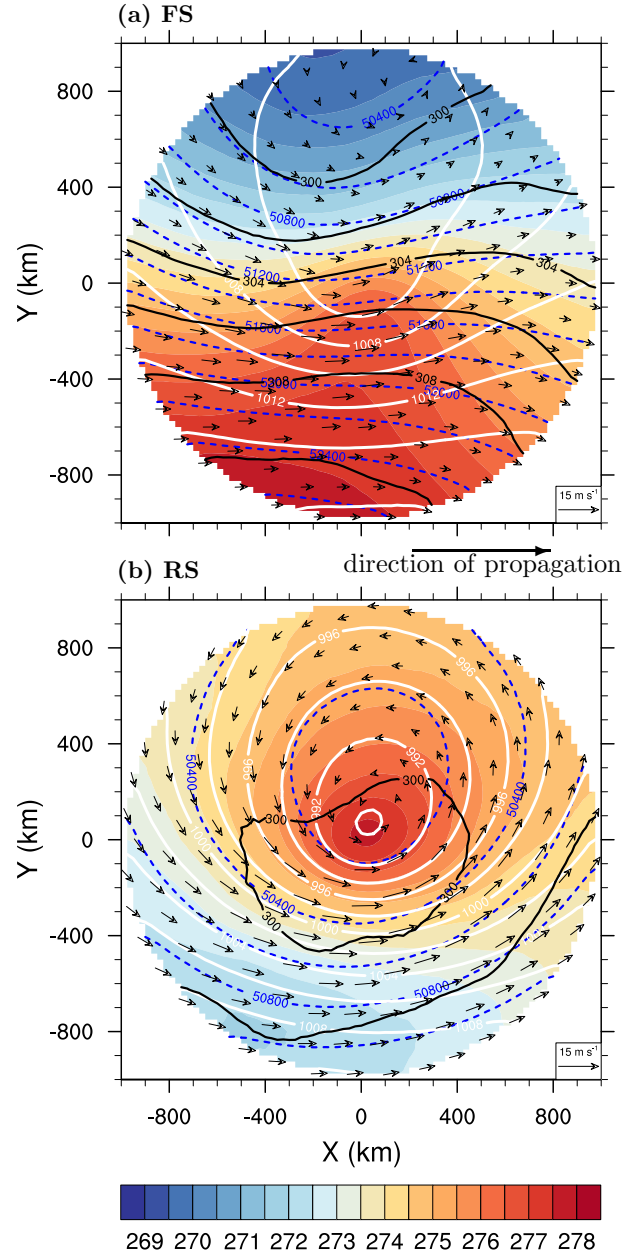
907 FIG. 4. (a) Number of PMCs per extended winters and (b) per month. The black line corresponds to all PMCs
 908 (ALL). The blue (red) lines correspond to PMCs formed in forward (reverse) shear conditions (FS, RS). (b) The
 909 dashed lines show +/- one standard deviation around each point.



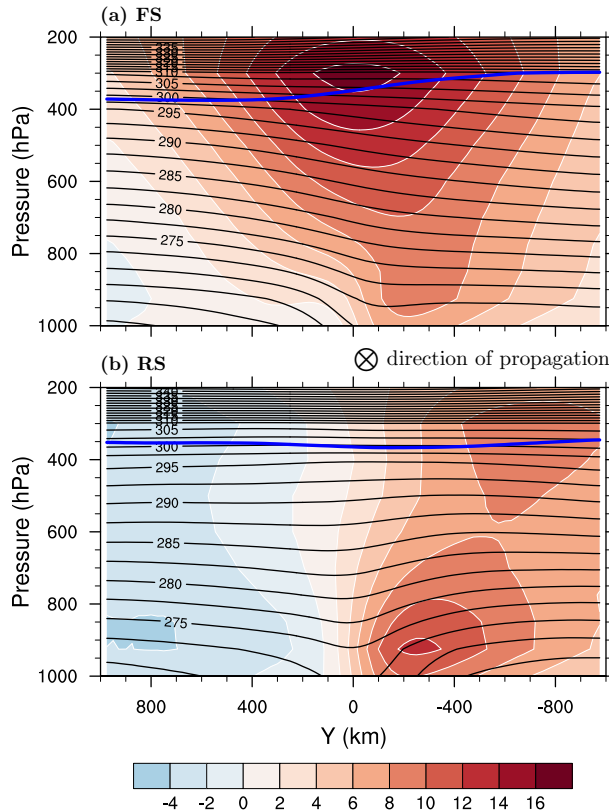
910 FIG. 5. Propagation direction frequency (length of the pieces) along with the propagation speed (shading,
911 unit: m s^{-1}) for (a-c) PMCs developing during forward shear (FS) conditions and (d-f) in reverse shear (RS)
912 conditions. In (a,d), no threshold in SST-T500 is applied to select the tracks. For (b,e) (c,f), only the tracks for
913 which $\text{Max}(\text{SST-T500}) > 46$ (< 40) are used. $\text{Max}(\text{SST-T500})$ is defined in the text.



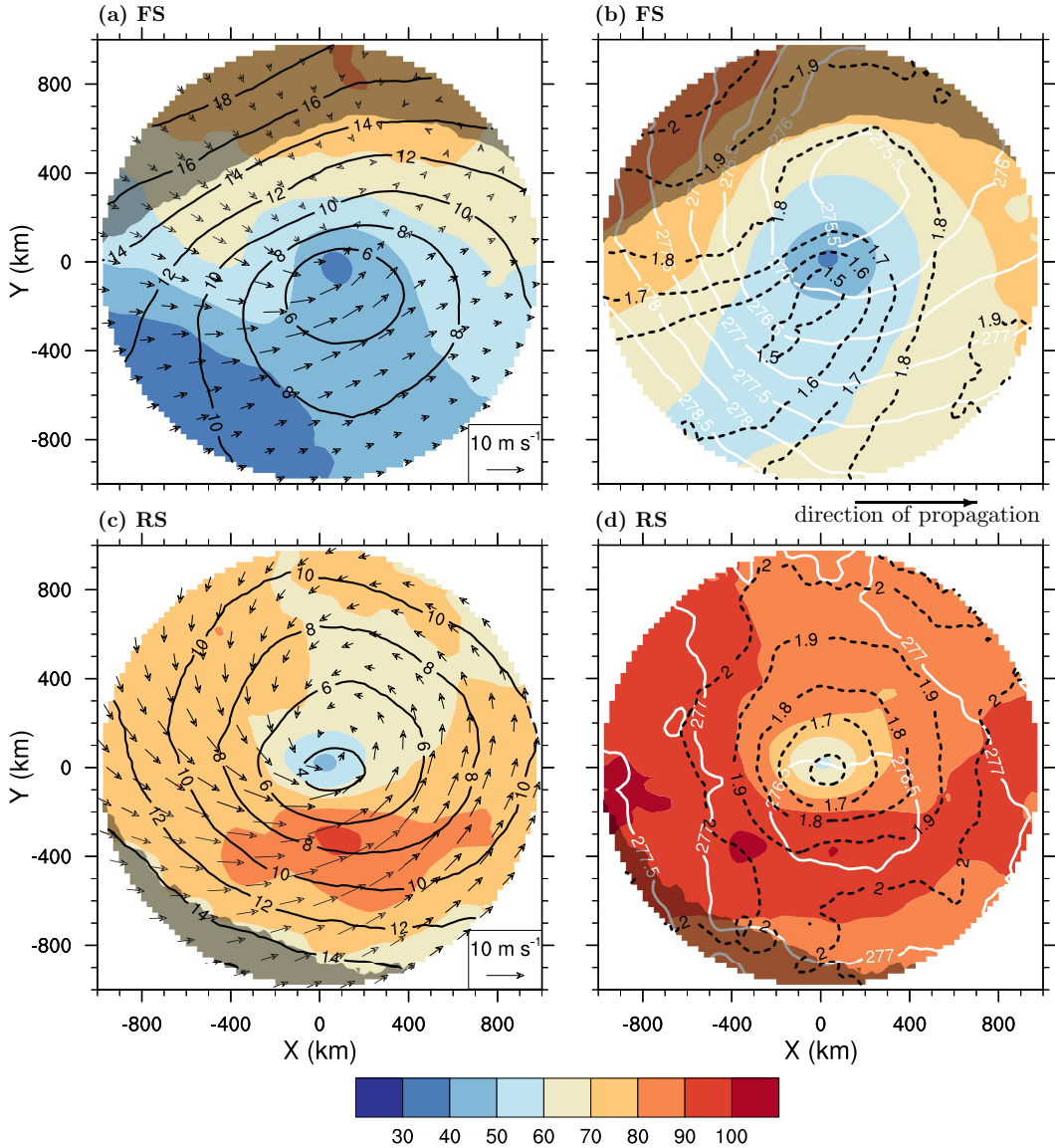
914 FIG. 6. (a,b) Geopotential at 500-hPa (black contours, interval: $500 \text{ m}^2 \text{ s}^{-2}$) and potential temperature at the
 915 tropopause defined by the 2-PVU surface (shading, unit: K) averaged over the genesis dates of PMCs. (c-f)
 916 Temperature at 850 hPa (shading, unit: K), wind at 850 hPa (arrows), and sea ice concentration (black line)
 917 corresponding to a value of 0.5) averaged over the genesis dates of PMCs. (a,c) Fields averaged for PMCs
 918 formed in forward shear (FS) conditions and (b,d) reverse shear (RS) conditions. (e) (f) Fields averaged for
 919 PMCs formed in FS conditions and having $\text{Max}(\text{SST-T500}) > 46$ (< 40). The solid (dashed) blue lines represent
 920 the 99% (95%) confidence levels calculated using a bootstrap method with (a,b) the 500-hPa geopotential and
 49 (c-f) the 850-hPa temperature.



922 FIG. 7. Composites of potential temperature at 850 hPa (shading, unit: K), wind at 850 hPa (arrows), geopo-
 923 tential at 500 hPa (dashed blue contours, interval: $200 \text{ m}^2 \text{ s}^{-2}$), potential temperature at 2 PVU (black contours,
 924 interval: 2 K), and mean sea level pressure (white contours, interval: 2 hPa) for the genesis time of (a) PMCs
 925 forming in forward shear (FS) conditions and (b) in reverse shear (RS) conditions. The direction propagation is
 926 towards increasing X values.



927 FIG. 8. Cross-sections in the direction of propagation of the wind (shading, unit: m s^{-1}), potential temperature
 928 (black contours, interval: 5 K), and the tropopause defined as the 2-PVU surface (blue line) composed for the
 929 genesis times of (a) PMCs formed in forward shear (FS) conditions, and (b) in reverse shear (RS) conditions.
 930 The positive (negative) values of Y represent the left (right) side relative to the propagation direction which is
 931 directed into the page.



932 FIG. 9. Composites of sensible (a,c) and latent (b,d) heat fluxes (shading, unit: W m^{-2}) for genesis time of
 933 PMCs during (a,b) forward shear (FS) conditions and (c,d) reverse shear (RS) conditions. Overlaid are (a,c)
 934 difference between SST and 2-m temperature (solid lines, unit: K) together with 10-m wind (arrows) and (b,d)
 935 SST (white solid contours, unit: K) together with the difference between specific humidity at 2 m and saturation
 936 specific humidity using SST (dashed contours, unit: g kg^{-1}). Values over 50% sea ice concentration or over land
 937 are omitted in the composites and areas are shaded where this omission occurs in more than half of the PMC
 938 cases. The direction of propagation is towards increasing X values. A nine-point local smoothing is applied to
 939 the fields after compositing.

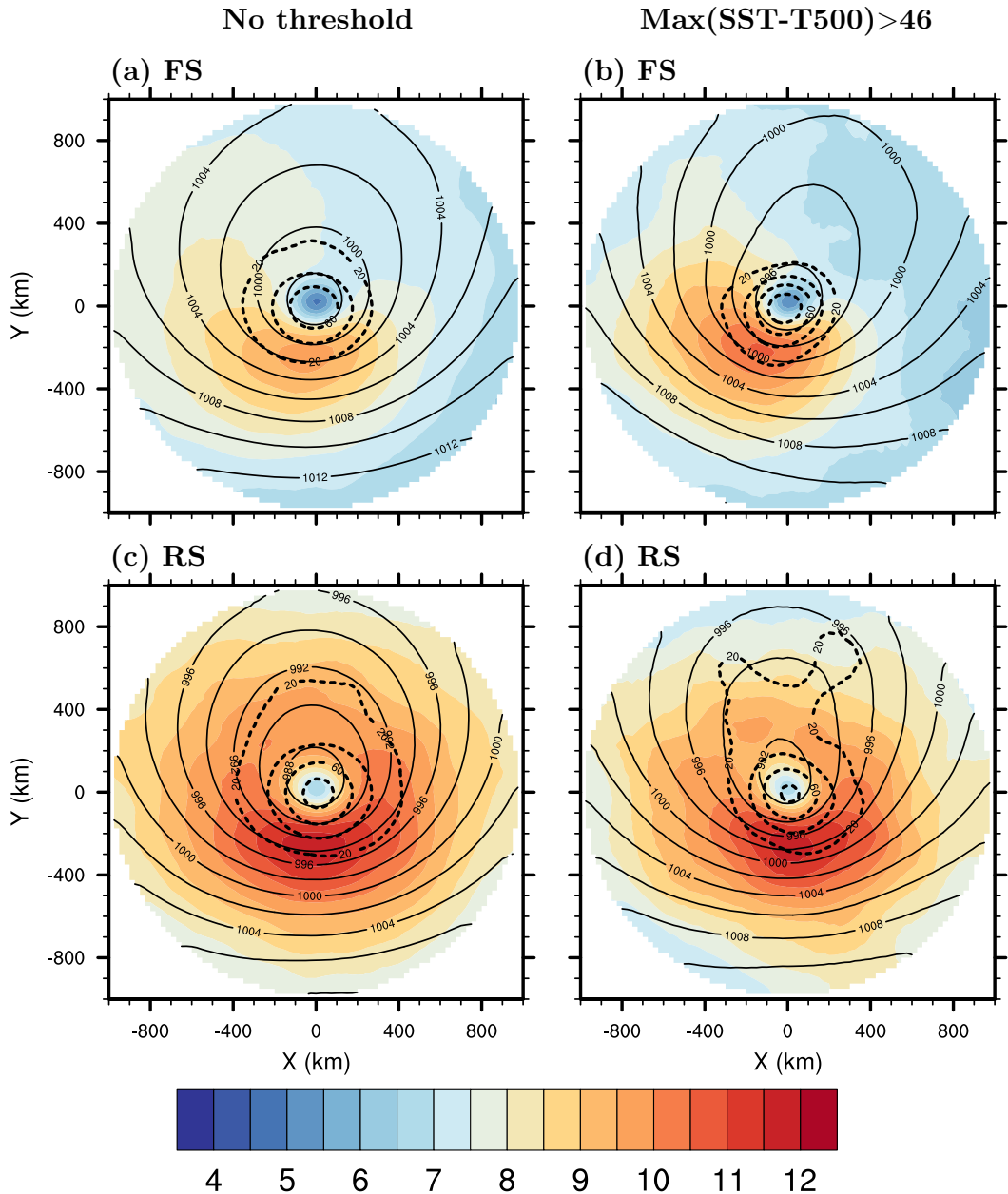
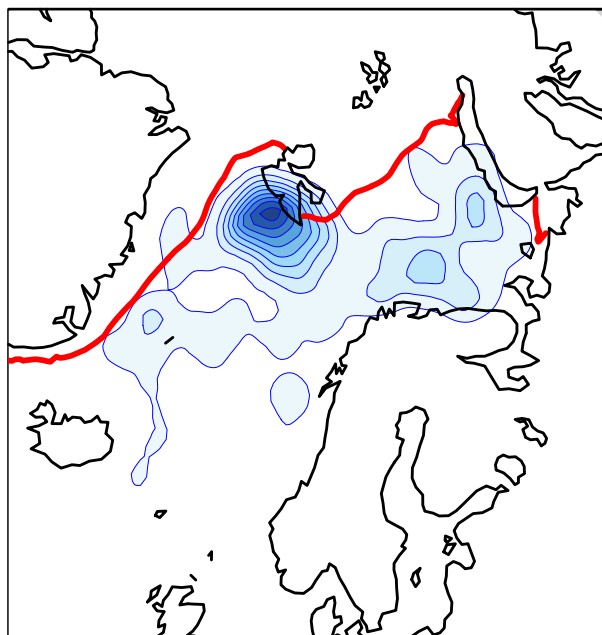
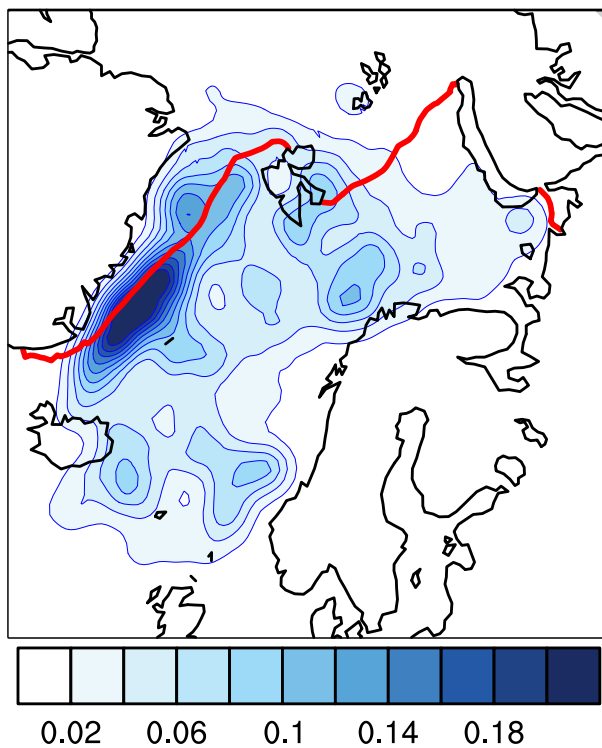


FIG. 10. Composites of the 10-m wind speed (shading, unit: m s^{-1}), mean sea level pressure (solid black contours, interval: 5 hPa), and relative vorticity at 850 hPa (dashed black contours, unit: 10^{-6} s^{-1} , interval: $20 10^{-6} \text{ s}^{-1}$) for the mature stage of PMCs formed in (a,c) forward shear (FS) conditions and (b,d) reverse shear (RS) conditions. For (a,c) no threshold in SST-T500 is applied to the tracks. For (b,d) only tracks with $\text{Max}(\text{SST-T500}) > 46$ are used. The propagation direction is towards increasing X values. The mature stage is defined as the time for which the mean sea level pressure reaches its lowest value during the cyclone lifetime.

946 (a) FS, $\text{Max}(\text{SST-T500}) > 46$

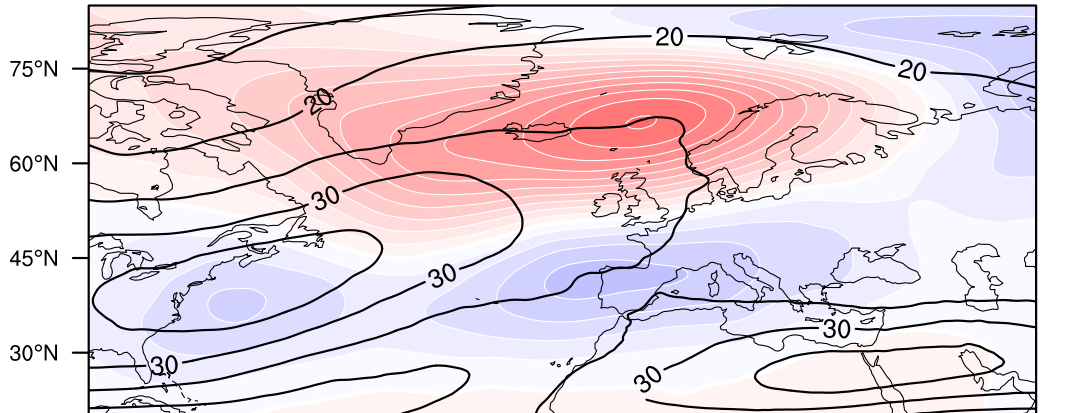


947 (b) FS, $\text{Max}(\text{SST-T500}) < 40$

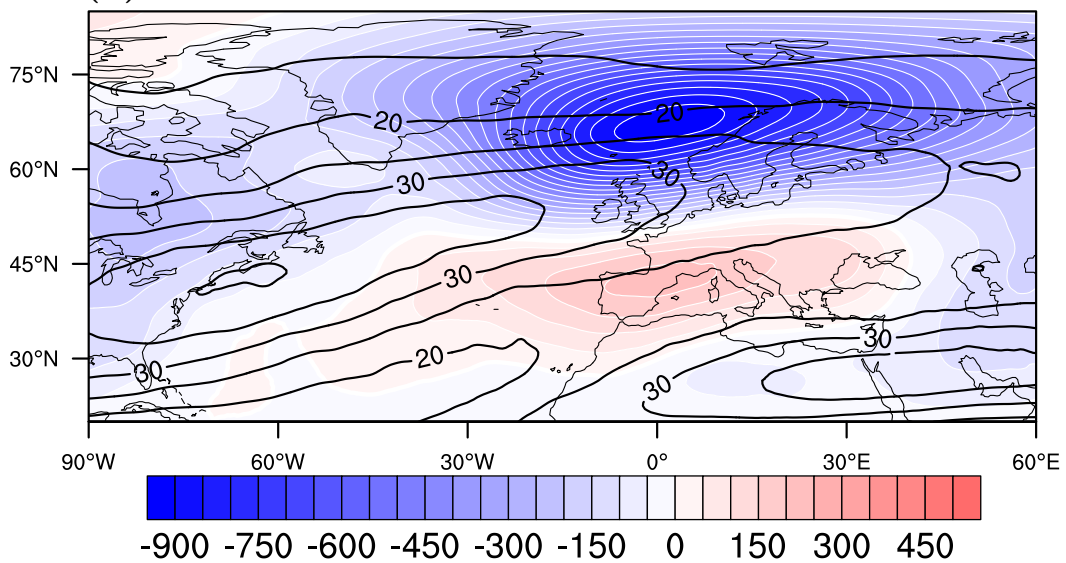


946 FIG. 11. Cyclogenesis densities for PMCs forming in forward shear conditions and having (a) $\text{Max}(\text{SST-T500}) > 46$ and (b) $\text{Max}(\text{SST-T500}) < 40$. Unit is a number of polar lows per extended winter per 10^4 km^2 .
947

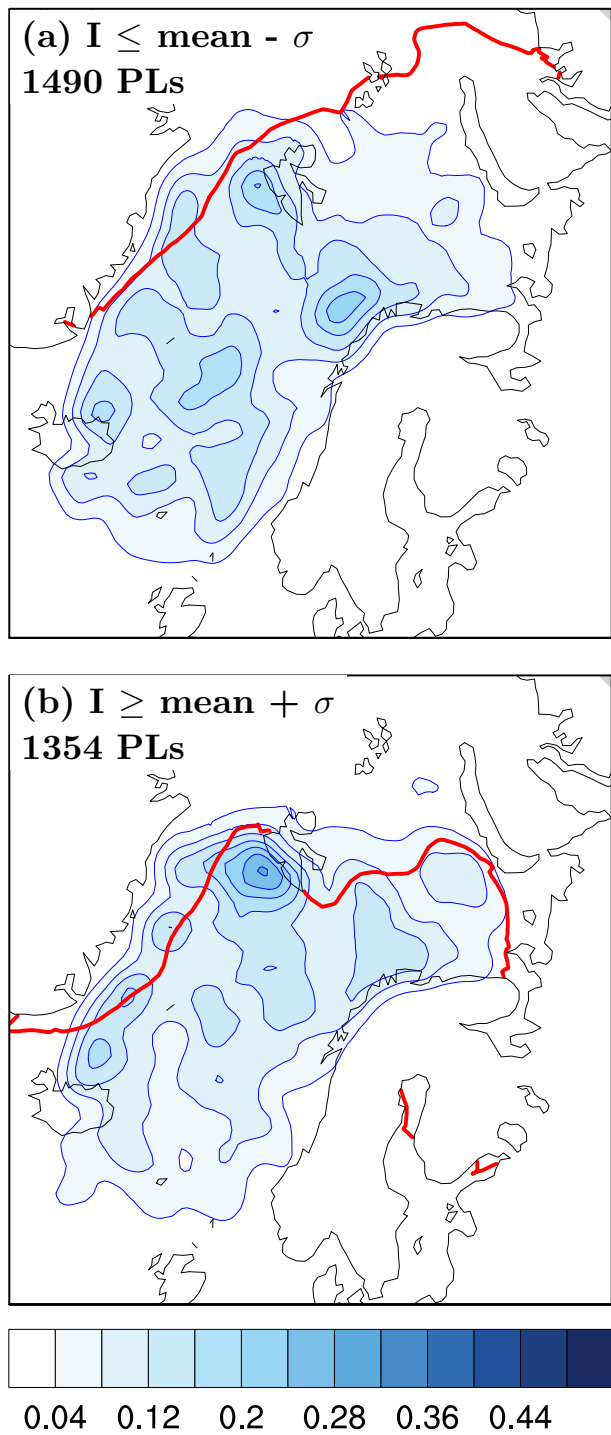
(a) FS



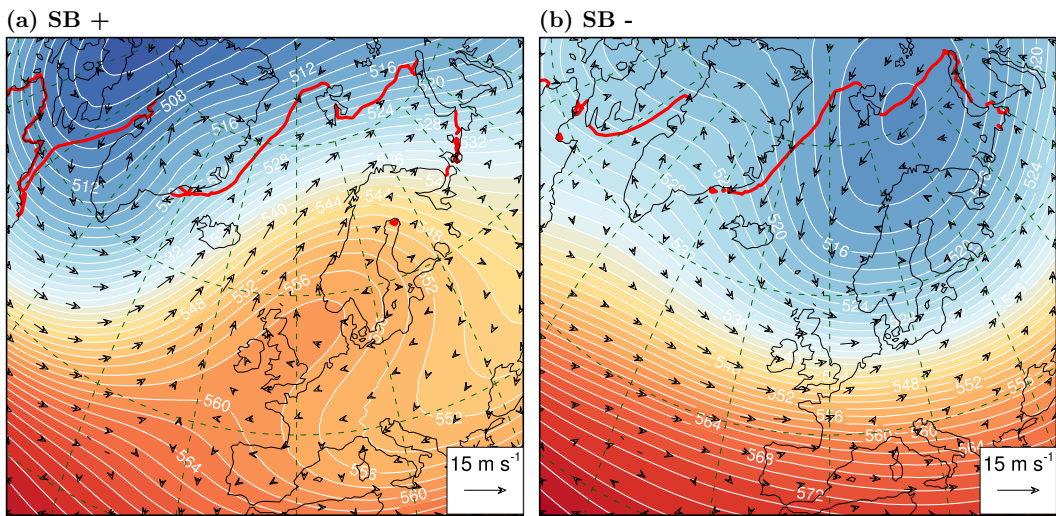
(b) RS



948 FIG. 12. Composites of the wind speed at 300 hPa (black contours, interval: 5 m s^{-1}) and the 500-hPa
949 geopotential anomalies relative to the extended wintertime climatology (shading, unit: $\text{m}^2 \text{ s}^{-2}$) for the genesis
950 times of PMCs formed in (a) forward shear (FS) conditions and (b) reverse shear (RS) conditions.



951 FIG. 13. Cyclogenesis density of PMCs for the Arctic sea ice extent index (a) (b) lower (greater) than its mean
 952 minus (plus) one standard deviation. Unit is number of PMCs per extended winter per 10^4 km^2 . The red line
 953 represents 50% sea ice concentration.



954 Fig. B1. Composites of the (a) positive and (b) negative phases of the Scandinavian Blocking of the 500-hPa
 955 geopotential (shading, unit: dam), 10-m wind (arrows) and the 50% sea ice concentration contour (red line) for
 956 the period 1979-2014. The positive (negative) phases are defined as the days for which the index is higher
 957 (lower) than the mean plus (minus) one standard deviation.